

Aug. 01 2009 version

Emission from a Young Protostellar Object I. Signatures of Young Embedded Outflows

Masako Yamada

*Institute of Astronomy and Astrophysics, Academia Sinica, P. O. Box 23-141, Taipei,
10617, Taiwan, R.O.C.*

masako@asiaa.sinica.edu.tw

Masahiro N. Machida¹

*Department of Physics, Graduate School of Science, Kyoto University, Sakyo-ku, Kyoto,
606-8502*

Shu-ichiro Inutsuka

Department of Physics, Nagoya University, Furo-cho, Chikusa-ku Nagoya, 464-8602

and

Kohji Tomisaka²

*Division of Theoretical Astronomy and Center for Computational Astronomy, National
Astronomical Observatory of Japan, Osawa, Mitaka, Tokyo, 181-8588*

ABSTRACT

We examine emission from a young protostellar object (YPO) with three-dimensional ideal MHD simulations and three-dimensional non-local thermodynamic equilibrium (non-LTE) line transfer calculations, and show the first results. To calculate the emission field, we employed a snapshot result of an MHD simulation having young bipolar outflows and a dense protostellar disk (a young circumstellar disk) embedded in an infalling envelope. Synthesized line emission

¹present address: Division of Theoretical Astronomy and Center for Computational Astronomy, National Astronomical Observatory of Japan, Osawa, Mitaka, Tokyo, 181-8588

²also at School of Physical Sciences, Graduate University for Advanced Studies (SOKENDAI).

of two molecular species (CO and SiO) show that subthermally excited SiO lines as a high density tracer can provide a better probe of the complex velocity field of a YPO, compared to fully thermalized CO lines. In a YPO at the earliest stage when the outflows are still embedded in the collapsing envelope, infall, rotation and outflow motions have similar speeds. We find that the combined velocity field of these components introduces a great complexity in the line emissions through varying optical thickness and emissivity, such as asymmetric double-horn profiles. We show that the rotation of the outflows, one of the features that characterizes an outflow driven by magneto-centrifugal forces, appears clearly in velocity channel maps and intensity-weighted mean velocity (first moment of velocity) maps. The somewhat irregular morphology of the line emission at this youngest stage is dissimilar to a more evolved object such as young Class 0. High angular resolution observation by e.g., the Atacama Large Millimeter/submillimeter Array (ALMA) telescope can reveal these features. Our results demonstrate a powerful potential of the synthesized emission of the three-dimensional line transfer to probe the velocity field embedded in the envelope, and further analysis will be able to determine the precise velocity field to assess the dynamics in the young protostellar object to gain a better understanding of star formation.

Subject headings: stars: formation — ISM : jets and outflows — radiative transfer — radio lines : stars – submillimeter

1. Introduction

The formation of stars begins with the collapse of a parent dense molecular core. As gravitational collapse of a molecular core proceeds, bipolar outflows are expected to form in relation to accretion and rotation of the parent core. Observations of the embedded, young Class 0 objects revealed that some of them exhibit infall and rotational motions in emission profiles as well as bipolar outflows (see e.g., Belloche et al. 2002 for IRAM 04191; Bourke et al. 2005 for L1041-IRS; Matthews et al. 2006 for Bernerd 1-c). The velocity structure in the stage prior to Class 0 objects, before the formation of a protostar, is expected to represent the dynamics in the earliest phase of star formation. Therefore, the observational studies of the very young stage of star formation, on the way from a prestellar (starless) core to a Class 0 object, are quite important in understanding the star formation processes. We further can expect a hint of a launching mechanism of molecular outflows, almost free from the propagation effect, in the earliest stage of star formation.

Before a protostar begins to shine, temperature of the star-forming object without a

heating source is as quite low as 10 K. Major observational ways are thus molecular emission lines in the millimeter and submillimeter bands. After a protostar forms, the young object at the earliest stage of star formation (hereafter “a young protostellar object” or a YPO for simplicity) has: 1) a vast amount of envelope matter, 2) complex velocity structure consisting of infall, rotation, and outflow motions, and 3) a complicated optical thickness structure due to the complex velocity field in the millimeter and submillimeter bands. As a result, it is not an easy task to correctly interpret the complex velocity field imprinted in the emergent line emission. Furthermore, current observational facilities do not achieve sufficient angular resolution to resolve the varying velocity field within the molecular core. However, forthcoming high angular resolution observations provided by the Atacama Large Millimeter/submillimeter Array (ALMA) will be able to reveal these internal structures of an evolving core, and a significant progress in understanding the star formation process is expected. In addition, the launch of the *Herschel* satellite will enable observations with high frequency resolution in the submillimeter (and shorter wavelength) band. For these new observational facilities, detailed modelling and understanding of the radiation field of young star forming objects is of crucial importance. In this regard, prestellar cores have been studied with one-dimensional hydrodynamic model and radiative transfer calculations (e.g., Pavlyuchenkov et al. 2008; Tsamis et al. 2008). Here, we employ a theoretical model constructed with a three-dimensional, high resolution numerical simulation of the formation process of a protostar (Machida et al. 2008). By combining it with three-dimensional, non-local thermodynamic equilibrium (non-LTE) line transfer calculations, we examine a characteristic feature in the radiation field of a YPO. In this article, we show the first results in formats common to radio observers. Feasibility evaluation of these synthesized emissions by the ALMA telescope is another interesting problem, but we do not treat it in detail in this article except for simple estimates of the necessary exposure time.

The outline of this article is as follows. In §2, we describe the models and the set-ups of the magnetohydrodynamic and radiative transfer simulations. The results of continuum and molecular line emissions are presented in the same formats used in radio observations in §3. We make comments with regard to observations with current and future observational facilities and discuss them in §4. Summary and conclusions are presented in §5.

2. Models and Simulations

2.1. Magnetohydrodynamic Modelling

Evolution from a parent dense molecular core to a protostar proceeds with a several characteristic evolutionary stages (see e.g., Masunaga & Inutsuka 2000, and their Figure

2b). At the onset of collapse, cooling by dust emission is so effective within a molecular core that it contracts nearly isothermally with an initial low temperature. Gravitational contraction proceeds and the central density increases, until the core becomes optically thick to the dust thermal emission. At this stage the cooling rate is less efficient and the collapse becomes adiabatic at the density of $n \sim 10^{11} \text{ cm}^{-3}$. At this point an adiabatic core of a radius $R \sim 1 - 10 \text{ AU}$ and a mass $\sim 0.01M_{\odot}$ surrounded by the accretion shock is formed at the center. This core is called “the first core” (Larson 1969). The kinetic temperature, T_{kin} , increases as the first core contracts adiabatically. When T_{kin} exceeds $\sim 2000 \text{ K}$, hydrogen molecules begin to dissociate. Since dissociation is an endothermic process, the equation of state becomes soft again, and it induces dynamical contraction of the central region at $n \gtrsim 10^{16} \text{ cm}^{-3}$ (second collapse). Once all the hydrogen molecules are dissociated, the equation of state becomes adiabatic again, and eventually a second core (protostar) is formed.

Considering this picture, we employed the MHD modelling of Machida et al. (2008) as one among those most plausible and based on detailed calculations. Machida et al. (2008) investigated the evolution of a star-forming object from a parent dense molecular core to a protostar by three-dimensional resistive MHD simulations. They showed that the magnetic force working in an evolving core can naturally drive a slow and wide opening angle flow of $\sim 5 \text{ km s}^{-1}$ and a fast and collimated flow of $\sim 30 \text{ km s}^{-1}$ from the first and second cores, respectively. In their scenario, these two flows are expected to increase their velocities and evolve to a molecular bipolar outflow ($v \gtrsim 10 \text{ km s}^{-1}$) and an optical jet ($v \gtrsim 100 \text{ km s}^{-1}$) as observed in more evolved young stellar objects (YSOs). In this article, we follow their scenario and simply refer to the low-velocity flow formed in their calculations as an “outflow”. Observational study of protostellar objects and outflows in their earliest evolutionary stage is indeed quite important for a comprehensive understanding of the star formation process as well as for the theoretical modelling. Since the characteristic structures of the youngest star-forming objects are small in size, they will be a milestone target of special interest of the ALMA telescope.

Machida et al. (2008) showed that ideal and resistive MHD modelings do not introduce a significant difference in the onset of molecular outflows around the first core. In this study,

we calculated the cloud collapse based on the ideal MHD equations:

$$\frac{\partial \rho}{\partial t} + \nabla \cdot (\rho \mathbf{v}) = 0, \quad (1a)$$

$$\rho \frac{\partial \mathbf{v}}{\partial t} + \rho (\mathbf{v} \cdot \nabla) \mathbf{v} = -\nabla P - \frac{1}{4\pi} \mathbf{B} \times (\nabla \times \mathbf{B}) - \rho \nabla \phi, \quad (1b)$$

$$\frac{\partial \mathbf{B}}{\partial t} = \nabla \times (\mathbf{v} \times \mathbf{B}), \quad (1c)$$

$$\nabla^2 \phi = 4\pi G \rho, \quad (1d)$$

where ϕ denotes gravitational potential, and other symbols are used for usual meanings.

In order to calculate a model in a wide dynamic range, a nested grid method is adopted (see for details Machida et al. 2005). In this scheme, a rectangular grid of each level has the same number of grid points ($128^2 \times 64$), and cell width $h(l)$ varies with the grid level l . The width of a cell $h(l)$ decreases to a half the width of that of the previous grid level ($h(l-1)$). A new finer grid is generated whenever the minimum local Jeans length λ_J decreases below $8h(l_{\max})$ (thus the so-called Jeans condition of Truelove et al. 1997 is always satisfied in our simulation). We set the maximum and minimum grid level to $l_{\max} = 10$ and $l_{\min} = 1$. The grid of $l = 10$ has a spatial coverage of 250 AU and a cell width of 2 AU. Then our calculation can examine the first core and its vicinity with 2 AU at the highest resolution.

We adopt a critical Bonnor-Ebert sphere of $M = 0.6 M_{\odot}$, $R = 2000$ AU with a uniform kinetic temperature $T_{\text{kin}} = 10$ K as an initial condition. A uniform magnetic field of $B = 4.2 \times 10^{-5}$ Gauss threads the initial critical Bonnor-Ebert sphere. Initially the cloud rotates rigidly with dimensionless angular speed $\omega \equiv \Omega_0 / (4\pi G \rho_0)^{1/2} = 0.3$ (where $\Omega_0 = 5.4 \times 10^{-13}$ s $^{-1}$ is the initial angular speed and $\rho_0 = 3.8 \times 10^{-18}$ g cm $^{-3}$ or $n_0 = 10^6$ cm $^{-3}$ is the initial central density). We increased the initial density by 70% to induce gravitational collapse (see for more details, Machida et al. 2008).

For the thermal evolution, Machida et al. (2008) employed the barotropic relations $P(\rho)$ based on the equation of state of a one-dimensional radiative hydrodynamic simulation study of Masunaga & Inutsuka (2000). In this paper, we perform a non-LTE line transfer simulation with a numerical scheme optimized for a uniform Cartesian grid as a postprocessing procedure, making use of a snapshot data of the hydrodynamic simulation result of the nested grid scheme. In order to maintain a balance between preserving information obtained by the nested grid simulation having a fine grid in the innermost region and grasping a large scale feature of a whole system, we added a slight modification to the equation of state. In particular, we artificially raised the polytropic index after $n > 10^{14}$ cm $^{-3}$ to $\gamma = 2$, and stopped further contraction beyond $n > 10^{14}$ cm $^{-3}$ (see Eq.[5] of Machida et al. 2008 for comparison). The following set of barotropic relations $P(\rho)$ was used in the form of a

piecewise power-law,

$$P = \begin{cases} c_s^2 \rho & \rho < \rho_c, \\ c_s^2 \rho_c \left(\frac{\rho}{\rho_c} \right)^{7/5} & \rho_c < \rho < \rho_d, \\ c_s^2 \rho_c \left(\frac{\rho_d}{\rho_c} \right)^{7/5} \left(\frac{\rho}{\rho_d} \right)^2 & \rho_d < \rho, \end{cases} \quad (2)$$

where $c_s = 190 \text{ m s}^{-1}$ is sound speed at $T_{\text{kin}} = 10 \text{ K}$, $\rho_c = 1.92 \times 10^{-13} \text{ g cm}^{-3}$ ($n_c = 5 \times 10^{10} \text{ cm}^{-3}$) and $\rho_d = 3.84 \times 10^{-10} \text{ g cm}^{-3}$ ($n_d = 1.0 \times 10^{14} \text{ cm}^{-3}$), respectively. Due to this modification, the evolution of low speed outflows from just outside the first core can be calculated for a relatively long timescale. A similar technique was used in the numerical study of Tomisaka (2002).

As is described in detail in the next subsection (§2.2), we calculated emission from the model YPO separately from the magnetohydrodynamic simulation. We made use of a part of ($l = 7$) snapshot data of magnetohydrodynamic simulation at $t = 4200 \text{ yrs}$ after the formation of the first core as an standard input to the radiative transfer code for a uniform Cartesian grid. Figure 1 shows the density structure used in the radiative transfer simulation. It reveals bipolar outflows extending to about 2000 AU, and a very compact and dense first core at the center. In the vicinity of the launching region of the outflows, a cavity structure exists around the central axis (z -axis), and a shell of a shape of a letter “U” surrounding it. At this stage the major axis of the first core is about $\lesssim 50 \text{ AU}$. In addition to the outflows, one can observe a disk-like structure with a radius $R \lesssim 1000 \text{ AU}$ and a scale height $\lesssim 200 - 300 \text{ AU}$. This disk-like structure also appears in the calculations of Machida et al. (2008) after a protostar forms. As described above, we did not explicitly calculate the evolution of the central region where density exceeds $n \gtrsim 10^{14} \text{ cm}^{-3}$. However, our long-term calculation effectively enables an examination of further evolution of accretion phase to a protostar over a large scale (Figure 1), though lack of spatial resolution prevents us from observing a protostar formation in a much smaller spatial scale than the minimum cell size ($\sim 10 \text{ AU}$). This disk-like structure is a protostellar disk in its earliest stage, and will evolve to a flatter and rotationally supported circumstellar disk (hereafter we refer to it as a “protostellar disk”; Hennebelle & Fromang 2008). To study the formation and evolution processes of a rotation-supported circumstellar disk we obviously need calculations of an even longer term evolution with higher resolution than the snapshot time adopted here. Since this article focuses on the larger scale of young molecular outflows so that emission distribution can reasonably be resolved by the ALMA telescope, such an exceptionally high resolution simulation is beyond the scope of this article. The protostellar disk is characterized by both infall and rotational motions. In order to examine how the emitting and/or absorbing matters outside the outflows affect the emergent line intensities, it is convenient to define regions of

different velocity structure, i.e., by the ratio of infall and rotation velocities. Hereafter in this article we denote the least dense gas surrounding the outflows and the protostellar disk as an “envelope”, which has only a small ratio of rotational to infall motion and low density ($n \lesssim 2.24 \times 10^6 \text{ cm}^{-3}$) in the computational domain.

2.2. Radiative Transfer Simulations

We calculate continuum and molecular line emission individually using the snapshot data of magnetohydrodynamic simulation described in the previous subsection (§2.1). For a continuum emission, we calculated thermal emission from dust grains with opacity of Hildebrand (1983) (see also Beckwith et al. 1990). For molecular lines, we performed three-dimensional non-local thermodynamic equilibrium (non-LTE) radiative transfer simulations with an algorithm based on Hogerheijde & van der Tak (2000) (see Wada & Tomisaka 2005). In the numerical calculation of radiative transfer, rate equations in statistical equilibrium,

$$n_J \sum_{J' \neq J} R_{JJ'} = \sum_{J' \neq J} (n_{J'} R_{J'J}), \quad (3)$$

$$R_{JJ'} = \begin{cases} A_{JJ'} + B_{JJ'} \bar{J} + C_{JJ'} & J > J', \\ B_{JJ'} \bar{J} + C_{JJ'} & J < J', \end{cases} \quad (4)$$

are solved in each cell in the simulation box. In equation (4), $A_{JJ'}$ and $B_{JJ'}$ are Einstein’s coefficients for spontaneous decay and radiative transitions, and $C_{JJ'}$ is for collisional transition rates from the energy level J to J' , respectively. Since almost all the hydrogen is in molecular form at this evolutionary stage, we can safely take molecular hydrogen as a collisional partner, and then $C_{JJ'}$ becomes

$$C_{JJ'} = n_{\text{H}_2} \gamma_{JJ'},$$

where n_{H_2} is number density of molecular hydrogen, and collisional coefficient $\gamma_{JJ'} \approx \langle v\sigma \rangle$ is taken from the database tables of Leiden University (LAMDA; Schöier et al. 2005). In order to calculate the mean intensity appearing in equation (4) $\bar{J} \equiv (4\pi)^{-1} \int I_\nu d\Omega$, we used a set of sampling rays passing through each cell with a random direction determined by Monte Carlo method. Typically the number of sampling rays for each cell is 220 in the simulations. As is inferred from Figure 1, radiation field becomes anisotropic, so we examined if the number of ray ($N_{\text{ray}} = 220$) is sufficient to incorporate the anisotropic radiation field by experiments with larger number of N_{ray} up to 420. We found only negligibly small differences in these results with relative precision less than 0.1%, and the central region where coincidence becomes worse than 10% for these runs occupies only a small fraction of 10^{-6} for low J lines and a few percent for the maximum J ($= 10$) in volume. We hence

concluded $N_{\text{ray}} = 220$ is sufficient to obtain reasonably correct results, and below we show results of $N_{\text{ray}} = 220$ runs.

The specific intensity along the sampling rays are calculated by integrating a standard radiative transfer equation,

$$\frac{dI_\nu}{d\tau} = -I_\nu + S_\nu, \quad (5)$$

where S_ν is the source function, and \bar{J} in a cell is obtained from the average of specific intensities along the sampling rays passing through the cell. The excitation temperature is calculated by iterative calculations of equations (4) and (5) until a self-consistent solution of energy level population n_J and mean intensity \bar{J} is obtained. We repeat the iterative calculations until the energy level populations n_J converge with relative precision of $\sim 10^{-6}$ between the present and former iterations (see for details Yamada, Wada & Tomisaka 2007). As shown below (§3), optical thickness becomes rather large in most of the lines we calculated. To avoid misunderstanding of slow convergence caused by the huge optical thickness as the final convergence of self-consistent radiation field, we calculated until the relative difference of $(i-1)$ -th and i -th energy level populations fell below 10^{-11} or less as an experiment (which is taken to be 10^{-6} as a canonical value in the present paper). Comparison with this longer calculation did not find any significant difference from the results with relative precision of 10^{-6} , and thus we concluded that the level of convergence 10^{-6} is precise enough to avoid false convergence.

Kinetic temperature of the snapshot result of hydrodynamic simulation is almost isothermal with a low temperature $T_{\text{kin}} = 10\text{K}$, but in a small region at the center T_{kin} reaches as high as 177 K. Then in order to include the possible energy level cascade from high- J levels (see for details, Appendix of Yamada, Wada & Tomisaka 2007), we examined two choices of maximum energy level $J_{\text{max}} = 10$ and 16. We found these two runs gave negligible difference of 0.1% or less for the levels $0 \leq J \leq 10$. Therefore in order to save computational time, we chose the maximum energy level $J_{\text{max}} = 10$ in all the runs in this article. Furthermore we confirm our solution by running two cases for each parameter set with different initial energy level populations of LTE and optically thin limit (van der Tak et al. 2005). We accept only solutions that meet the criteria that runs of two initial level population coincide with relative precision of $\lesssim 10^{-4}$ for both of n_J and source function S_ν . The coincidence of S_ν is necessary because of the radiative transition terms in equation (4), or photon trapping effect (Yamada & Tomisaka 2009).

We assume a Gaussian profile ϕ_ν for absorption coefficient α_ν only with pure thermal

broadening $\Delta\nu_{\text{th}} \equiv \nu_0/c\sqrt{(2k_B T_{\text{kin}}/m)}$,

$$\phi(\nu)d\nu = \frac{1}{\Delta\nu_{\text{th}}\sqrt{\pi}} \exp\left[-\frac{(\nu - \nu_0)^2}{(\Delta\nu_{\text{th}})^2}\right]d\nu, \quad (6a)$$

$$\int_0^{+\infty} \phi(\nu)d\nu = 1, \quad (6b)$$

where ν_0 is the frequency of local line center, and k_B is the Boltzmann constant, respectively. Doppler effect due to bulk velocity of fluid elements is incorporated through the frequency shift of locally estimated $\nu_0(\mathbf{v})$ in each fluid element. Observations of young YSOs such as Class 0 objects and molecular cores suggested relatively small turbulent motion compared with thermal width from the line profile analysis (Di Francesco et al. 2001; Belloche et al. 2002; Bourke et al. 2005). It is also observationally suggested that turbulent motion is subsonic in isolated starless cores (Myers 1983; Goodman et al. 1998; Caselli et al. 2002). The snapshot data we use in our radiative transfer simulation is at the evolutionary stage on the way from a quiescent starless core to a Class 0 object. Then we neglect turbulent broadening in the absorption profile $\phi(\nu)$.

The snapshot data from the magnetohydrodynamic simulation cover only a part of the computational domain spatially as well as temporally. The magnetohydrodynamic simulation described in §2.1 is calculated with a fine resolution ($dx = 2$ AU) by nested grids from $l_{\text{min}} = 1$ up to $l_{\text{max}} = 10$, but we used a set of $l = 7$ grid data as a standard. The spatial size of the numerical box of $l = 7$ grid is $\approx (2000\text{AU})^2 \times 1000\text{AU}$, which covers a whole outflow (see Figure 1). Precise calculation of emergent emissions from the YPO under consideration requires absorption and/or emission of the region outside of the $l = 7$ grid. However in this article, we assume the Cosmic Microwave Background (CMB) radiation of $T_b = 2.73$ K as a background radiation for simplicity, instead of approximate inclusion of outer part. Most of the lines in our calculations are optically thick, and thus the effect of this artificial assumption about background radiation are limited in a very narrow region close to the outer boundary of $l = 7$ grid. In order to estimate the effects of the outer envelope to the radiation field of $l = 7$ grid, we calculated the identical radiative transfer simulation for $l = 5$ grid data which covers a larger volume but has 4 times coarser spatial resolution than $l = 7$ grid. We confirmed that the mean line profiles of $l = 5$ calculations averaged over the field of view do not show qualitative differences from $l = 7$ calculations especially for mid- and high- J lines of SiO molecule. Although a full nested grid radiative transfer calculation is necessary to a precise evaluation, we conclude our results of $l = 7$ grid data do not suffer from the significant influence of the outer boundary for SiO lines. For ^{12}CO and its isotopologue lines they turned out to suffer from the outer boundary effect. Thus we will show $l = 5$ grid data results as well as the canonical $l = 7$ grid data results for ^{12}CO and its isotopologues.

We calculated rotational transitions of the representative molecules used in observations of molecular outflows (^{12}CO , ^{13}CO , C^{18}O and SiO). Among these molecules, we show in this article the results of ^{12}CO (and its isotopologues) as the most popular outflow tracer, and SiO as a representative of high density tracer molecule since the average density in our snapshot data is high ($\sim 10^6 \text{ cm}^{-3}$). The purpose of this article is to illustrate the characteristic features in the emission in relation to the dynamical evolution of YPOs and their velocity fields, rather than chemical evolution. So we assume a spatially uniform molecular abundance distribution. SiO molecules are in general considered to be formed by gas-phase reactions of Si atom desorbed from dust grain mantles in a shocked gas with high velocity $\gtrsim 25 \text{ km s}^{-1}$ (Caselli et al. 1997; Schilke et al. 1997), and thus they are regarded as a high-velocity shock tracer. However, in the early stage before frozen-out onto dust grains, SiO molecule can be formed in gas-phase reactions more than 10% of the initial Si abundance in a short timescale 10^4 yrs before frozen-out dust onto grains (Langer & Glassgold 1990). Additionally, observation showed that in some outflows the location of the brightest SiO emission does not coincide with the location of the strongest terminal shock (e.g. HH 211: Hirano et al. 2006), and lower-velocity components than 25 km s^{-1} have been detected (e.g., Codella et al. 1999; Gibb et al. 2004). These facts implies that the formation mechanism of SiO molecule in protostellar objects remains still ambiguous (Arce et al. 2007). Then in order to prevent possible uncertainties in a specific chemical evolution model, we treat the abundance distribution as a free parameter in the numerical experiments. Since CS would be less sensitive to shock, and it has similar critical densities and wavelengths as SiO , the emission of CS lines resemble that of SiO in our calculations with uniform abundance. We will show CS results based on the chemistry models in future. HCO^+ will also be examined in the future article as a charged molecule. We take molecular abundances relative to hydrogen molecule as $y_{\text{CO}} = 3 \times 10^{-4}$ and $y_{\text{SiO}} = 2 \times 10^{-8}$ as fiducial values.

3. Results

In this section we present our simulation results analyzed in usual methods in radio observation. Spectral energy distribution (SED) of continuum emission, maps of synthesized molecular line intensities integrated along the line-of-sight velocity, position-velocity diagrams, channel maps, and line profile maps are presented. While we mainly consider high angular resolution observations with the ALMA telescope, we focus on the qualitative features in the synthesized radiation field because of the limitation of our simulation set-ups (see discussion in §2). That is, we do not include any response of realistic observation instruments by, for example, beam convolution and so forth. We also neglect atmospheric or system noises for the same reason.

3.1. Continuum: Thermal Emission from Dust Grains

Theoretically, continuum observation is easier to achieve a higher signal-to-noise ratio in high angular resolution observation in comparison to lines. We calculated the thermal emission from dust grains in hope of revealing smaller internal structures compared to line emission.

In the snapshot under consideration, the density is as high as $n \gtrsim 10^6 \text{ cm}^{-3}$, and we can assume a tight coupling between the gas and dust grains. As the kinetic temperature of gas is nearly isothermal ($T_{\text{kin}} = 10 \text{ K}$) except for a compact region around the first core at the center, we can take the dust temperature $T_d = T_{\text{kin}} \simeq 10 \text{ K}$. Then dust thermal emission is written as (Hildebrand 1983; Beckwith et al. 1990)

$$I_\nu = B_\nu \{1 - \exp(-\tau_\nu)\}, \quad (7)$$

$$\tau_\nu = \int \mu m_p n \kappa_\lambda dl, \quad (8)$$

$$\kappa_\lambda = 0.1 \left(\frac{0.25 \text{ [mm]}}{\lambda} \right)^\beta \text{ cm}^2 \text{ g}^{-1}, \quad (9)$$

where B_ν is Planck function, μ is the mean molecular weight, m_p is proton mass, dl is a line element along the line of sight, respectively. In our calculation we take $\beta = 2$ as a fiducial value. Figure 2 shows distributions of thermal emission of $T_d = 10 \text{ K}$ dust grains in terms of brightness temperature $T_b \equiv c^2/(2\nu^2 k_B) I_\nu$. Five panels correspond to different frequencies, $\nu = 150, 220, 350, 650, \text{ and } 850 \text{ GHz}$ falling in the band ranges of ALMA receivers. We take a single value of inclination angle of the outflow axis to the plane of the sky $\theta = 30^\circ$ (see a bottom right illustration for definition of θ) in Figure 2. We found that average physical quantities such as mean intensity do not strongly depend on θ , except for the morphology of intensity contours that follow the column density distribution.

The region bright in dust emission is mainly the central part of the protostellar disk that has high column density up to $\lesssim 10^{23} \text{ cm}^{-2}$. Panels (c), (d), (e) of Figure 2 show a weak structure of “X”-shape extending from the rim of a box-shape image of the protostellar disk. These are base of the slow speed outflows of a wide opening-angle (see Figure 1). These structures along the outflows are seen clearer in closer view to the edge-on of the protostellar disk (i.e. small θ), and are hidden by the geometrically thick protostellar disk at $\theta \gtrsim 60^\circ$ (close to the pole-on view). Note that since the intensity range shown in Figure 2 is restricted for a clear view, the contrast between intensities of the outflow cavity wall and the protostellar disk is more emphasized compared with the true values. Feasibility of detection of the signatures from the outflow cavity in dust emission depends on several factors actually, such as sensitivity of a telescope and gas-to-dust ratio in the outflow, and

requires more detailed investigation. Figure 2 shows that the brightness temperature of dust continuum emission is not strong (~ 0.02 K for 350 GHz), but a huge bandwidth (two polarization channels of 8 GHz) of receivers of the ALMA telescope enables the detection of these emission easily: for 2 mK sensitivity, the required observation time amounts to about 2.6 hours for an object at the distance of 140 pc and -30° declination with 0.3 arcsecond resolution.¹ For 850 GHz with 1.0 mK sensitivity, required time will be about 8.8 hours, which is possible and reasonable to carry out.

Figure 2 shows that the emission of higher frequency is brighter, whereas equation (9) also implies an increase in optical thickness with frequency. Finite optical thickness moderates the increase in intensity (Eq. [7]) compared to the optically thin regime. In Figure 2 (c), (d) and (e), we indicate the thick ($\tau_\nu \geq 1$) regions of $R \sim 20 - 100$ AU with solid black contours at the center. One can see that though τ_ν increases with frequency, the region of $\tau_\nu \geq 1$, in which correction is needed in conversion from T_b to column density, is confined in a very small region at the center. As described in §2.1, we have to consider the outer region surrounding the $l = 7$ grid employed in our calculation for a more precise estimation. Table 1 summarizes the maximum and the mean optical thicknesses in the field-of-view defined by the computational domain ($l = 7$ grid). It also shows values for $\beta = 1.5$ and 1.

Continuum emission shows symmetric distribution with respect to the $x = 0$ axis ($y - z$ plane) and $z = 0$ axis ($x - y$ plane), reflecting symmetric density structure (Figure 1). This symmetry is greatly different from line intensity distribution discussed below (Figure 5). Panels (c) and (d) of Figure 2 show very weak emission from the narrow structure along the outflow axis. Although the dust emission can have information of the density structures other than the protostellar disk, it will be quite difficult to detect these weak emissions because of much brighter protostellar disk. In spite of our expectation of high angular resolution continuum observations, actual observation of dust emission will work as a measure of inclination angle of a protostellar disk and configuration of outflows, rather than examining the tiny launching region of outflows at the center. This is similar to what is done in current observations, indicating that we would not take advantage of the high resolution of the ALMA telescope. We plot average SEDs for three values of β (2, 1.5, and 1) in Figure 3. Since the protostellar disk is geometrically thick, mean intensity averaged over the field-of-view is almost independent of the inclination angle θ as well as azimuthal angle around the outflow axis ϕ , thus multi-band observations will be able to clearly determine β . Differences in SED by β appear stronger in longer wavelength regime where optical thickness effect is minimal.

¹We used the ALMA sensitivity calculator for the evaluation throughout the paper (<http://www.eso.org/sci/facilities/alma/observing/tools/etc/>).

3.2. Line Emission: A Probe of Velocity

In this subsection we show the results of non-LTE line transfer calculations. In contrast to the continuum emission, lines become a key to derive information of the velocity field which describes the characteristic features in the youngest evolutionary stage in star formation.

3.2.1. Excitation Status

In this subsection we examine excitation temperature. In Figure 4 we plot the excitation temperatures ($T_{\text{ex}}(ij) \equiv -h\nu_{ij}/k_B \{\ln(g_i/g_j) - \ln(n_i/n_j)\}^{-1}$, where g_i is statistical weight and $h\nu_{ij} \equiv E_i - E_j$) of SiO in each cell as a function of local density. Figure 4 shows that low- J transition in millimeter band the energy level population is almost fully thermalized ($T_{\text{ex}} \simeq T_{\text{kin}} \simeq 10$ K), while high- J transition (upper level of J , $J_{\text{upp}} \gtrsim 4$) in submillimeter band departs from LTE in the low density regime ($n \lesssim 10^7 - 10^8 \text{ cm}^{-3}$). This is due to the increasing critical density for LTE with J ($n_{\text{crit}} \approx 10^5 \times J^3 \text{ cm}^{-3}$ for SiO rotational transitions). The low density region ($n \lesssim 2 \times 10^6 \text{ cm}^{-3}$) roughly corresponds to the envelope and a part of the protostellar disk, and the high density region ($n \gtrsim 10^8 \text{ cm}^{-3}$) concentrates to the first core and a part of the midplane of the protostellar disk (see Figure 1). Therefore, for example, we can expect that $J = 4 - 3$ ($\nu_{43} = 173.883100$ GHz) lines will show non-LTE effects in the envelope, and $J = 7 - 6$ ($\nu_{76} = 303.9268092$ GHz) will show them in the envelope and the protostellar disk. We do not show a similar figure of ^{12}CO : because of lower critical density of ^{12}CO compared to SiO ($n_{\text{crit}} \approx 10^2 \times J^3 \text{ cm}^{-3}$), energy level population of ^{12}CO is almost completely thermalized up to the highest transition ($J = 10 - 9$) in our line transfer calculations.

3.2.2. Integrated Intensity

For a brief overview of the synthesized line emission distribution, first we show maps of integrated intensity of SiO(7 – 6) in Figure 5. In Figure 5, we overplot red and blue components in color lines on the total integrated intensity in gray scale, where intensities of total, “red component”, and “blue component” are defined with the line-of-sight projection

of the relative velocity with respect to the rest of the object v_r :

$$I_{\text{tot}} = \int_{-\infty}^{+\infty} T_b dv_r, \quad (10)$$

$$I_{\text{red}} = \int_0^{+\infty} T_b dv_r, \quad (11)$$

$$I_{\text{blue}} = \int_{-\infty}^0 T_b dv_r, \quad (12)$$

respectively. Four panels in Figure 5 are for different inclination angles ($\theta = 90^\circ$, 60° , 30° , and 0° for panels (a), (b), (c) and (d), respectively). Distributions of red and blue components can be described by superposition of rotation of the protostellar disk and the outflows, infall and outflow motions. The rotational motion causes symmetric distribution of red and blue components with respect to the $x = 0$ axis (except for $\theta = 90^\circ$ or pole-on view: see panels (c) and (d) of Figure 5), and infall and outflow motions give rise a symmetric distribution of them around the center (i.e., I_{red} is almost the same with I_{blue} at the location rotated by 180° around the center: panels (b) and (c) of Figure 5). Outermost contours surrounding the projected outflows in panels (b) and (c) become circular, because the envelope has nearly radial infall velocity.

Next we show the integrated intensity of ^{12}CO , ^{13}CO , and C^{18}O in Figure 6. As is discussed in §2.2, these molecules are more easily excited in the envelope compared with SiO, and hence the outer envelope surrounding the $l = 7$ grid cannot be neglected. Line transfer simulations of lower l grid data show that the photospheres of lines of these molecules are located just inside the radius of the initial Bonnor-Ebert sphere. We show $l = 5$ grid data results in Figure 6 ($\theta = 60^\circ$), which cover the whole initial Bonnor-Ebert sphere and thus the photospheres of CO and its isotopologues. In these figures we adopted molecular abundances y to be 2×10^{-4} , 2×10^{-6} , and 2×10^{-7} for ^{12}CO , ^{13}CO , and C^{18}O , respectively. Figure 6 shows that because of the large optical thickness (see Figure 7 below), intensity distributions have only weak structure compared with SiO (Figure 5). This result means that, due to the high density of the parent molecular core, even the rare isotopologue lines of CO becomes optically thick as well as ^{12}CO . In more evolved system, difference in the optical thicknesses in ^{12}CO and its isotopologues can be used to trace different components, but they are not good probe of emission signatures of the very young embedded YPO like that modelled in this article. Because the timescale of CO freeze-out is short in the high density core ($\sim 10^4$ yrs for $\gtrsim 10^6 \text{ cm}^{-3}$: e.g., Flower, Pineau des Forêts & Walmsley 2005), it may be possible that significant amount of gas phase CO is locked on the dust grains in the youngest YPO. If extremely effective depletion reduces the molecular abundance in the gas phase by a factor of 10^{-3} or less in the entire core, the signature of the embedded YPO would be easier to appear, but such a large factor of depletion is unlikely (see chemistry model, e.g., Aikawa et al. 2001).

If the YPO further evolves, emission from the central protostar will heat up the dust grains and desorb CO into gas phase again, and furthermore the dissociative background radiation might prevent CO molecule from freeze-out (e.g., Jørgensen et al. 2005, 2006). Taking into account these factors, the extremely strong CO depletion is unlikely in a real YPO, and our conclusion that CO and isotopologue lines are not useful to examine the kinematics of a YPO does not change, though absolute intensity and locations of photospheres would be slightly affected.

3.2.3. Average Line Profiles

Figure 7 plots line profiles of ^{12}CO emission averaged over the field-of-view for $l = 5$ grid calculations. Three panels show different transitions ($J = 1 - 0$, $2 - 1$, and $3 - 2$) for a fixed viewing angle $\theta = 60^\circ$. All three transitions display a strongly saturated line profile with very weak wing emission ($|v_r| \gtrsim 2 \text{ km s}^{-1}$). The strongly saturated profile is due to two facts: 1) in our computational domain the density is higher than critical densities for these lines ($n_{\text{crit}} \sim 10^2 \times J^3 \text{ cm}^{-3}$) and the energy level population is fully thermalized up to the maximum J ($=10$) in our calculation, and 2) resultant optical thickness becomes huge ($\tau_\nu \sim 1500 - 2500$ at the rest frequency; note the optical thickness becomes even larger if high resolution larger l data are correctly incorporated) as plotted with dashed lines in Figure 7. Considering possible depletion of ^{12}CO molecules on dust grains in the YPO, we performed numerical experiments with lower abundances ($y_{\text{CO}} = 3 \times 10^{-5}$ and 3×10^{-6}) using the same snapshot data. However, we could not find significant differences in line profiles even with a 100 times smaller molecular abundance. These imply that in our calculation of a YPO, energy level population of ^{12}CO is governed by collisional transitions and by a relatively small contribution from radiative transitions ($\propto B_{JJ'}$) in spite of large optical thickness. The same results apply to isotope molecules like ^{13}CO and C^{18}O . Note that as the very young protostellar object in our calculation evolves and forms a less dense and larger molecular outflow, optical thickness of ^{12}CO will significantly be reduced and the saturated profiles will disappear. The saturated profile in our results, which is not seen in current observations, appears because we calculated the emission from the compact high density region at the center of the computational domain.

In Figure 8 we plot average profiles of SiO lines in a similar way but for the canonical $l = 7$ data results. Since the optical thickness diminishes by a factor of 100 or more compared to ^{12}CO , the average profiles do not saturate but appear as a double-horn shape. Obviously SiO lines are better tracers to probe kinematics in the YPO under consideration compared with ^{12}CO (and its isotopologue) lines, besides chemical evolution in the very early stage that

has to be further investigated to conclude whether SiO is the *best* tracer. The double-horn profiles appear in all the maps with different inclination angles θ , including pole-on view with various degree of skewness in red and blue and varying depth of the dip at $v_r = 0$. From these arguments and Figures 7 and 8, radiative transitions ($\propto B_{JJ'}$) comparatively contribute in determining the energy level population of SiO molecule as collisional transitions. Like in the case of ^{12}CO , we performed numerical experiments of radiative transfer calculations with several lower molecular abundances down to $y_{\text{SiO}} = 2 \times 10^{-10}$, and confirmed that both intensities and profiles of SiO lines change according to the molecular abundance. Our results demonstrate that interpretation of subthermally excited lines along with chemical evolution should be done carefully.

3.2.4. Intensity Weighted Mean Velocity along the Lines of Sight

To display velocity structure clearer, we calculated the intensity-weighted mean velocity along the line of sight (or first order moment),

$$\langle v_r \rangle \equiv \frac{\int T_b v_r dv_r}{\int T_b dv_r}, \quad (13)$$

and show the distribution of $\langle v_r \rangle$ of SiO(7–6) line in Figure 9. As is seen in Figure 8, in our calculations the optical thickness of SiO is also large, though smaller than ^{12}CO . Then the intensity-weighted mean velocity $\langle v_r \rangle$ roughly traces velocity at $\tau \simeq 1$ region near the outer boundary, and hence it does not depend strongly on J . In Figure 9 three panels with different viewing angles ($\theta = 60^\circ$, 30° , and 0°) are presented. As is seen in Figure 9, $\langle v_r \rangle$ appears antisymmetric around the center in panels of $\theta = 60^\circ$ and 30° cases (i.e., $\langle v_r \rangle \simeq -\langle v_r \rangle$ at the position rotated by 180° around the center). There appears a quite characteristic pattern of peaks of $\langle v_r \rangle$ in “S” shape in these panels. These features originate in the rotation of the outflows around the outflow axis, which are driven by magneto-centrifugal force in the vicinity of the first core (e.g., Tomisaka 1998, 2000; Machida et al. 2008). If the outflow having a cavity rotates and inclines with respect to the plane of the sky, the total velocity component along the line of sight consists of flowing velocity along the outflow axis and rotation around the outflow axis. Opposite sign of rotation velocity in two sides of the outflow axis generates the gradients of $\langle v_r \rangle$ across the (projected) outflow axis with opposite signs in red and blue lobes. If the outflow axis is exactly in the plane of the sky, thus generated gradients in $\langle v_r \rangle$ maps appear with the same sign in the two lobes directing upwardly and downwardly, because the protostellar disk and the outflows rotate in the same direction. One can see

absence of the “S”-shape in the $\theta = 0^\circ$ map (panel (c) of Figure 9), where the outflow axis aligns exactly in the plane of the sky.

In order to demonstrate the effects of rotation of the outflow on line emissions clearer, we performed line transfer simulation with a modified snapshot data. We artificially set $v_\phi (\equiv \sqrt{v_x^2 + v_y^2}) = 0$ in the snapshot and put it as an input to the line transfer calculation. Figure 10 (b) shows the results of $v_\phi = 0$ run of SiO(4–3) line. The velocity gradients across the outflow axis disappear in the $v_\phi = 0$ run (panel (b) in Figure 10), while the original result of SiO(4–3) ($v_\phi \neq 0$) conserves the similar gradients as in Figure 9. These velocity gradients will be able to observationally confirmed with a spatial resolution of $\approx 100\text{--}200$ AU (required resolution depends on the inclination angle) and a velocity resolution of ≈ 0.1 km s $^{-1}$. If a YPO of this evolutionary stage is at a distance of 140 pc, 100 AU corresponds to $0.71''$, and above structure could be resolved with current instruments such as the Submillimeter Array.

In the case of CO, because of the locations of photospheres distant from the embedded outflow, $\langle v_r \rangle$ appears more weakly than SiO. Figure 11 shows the similar $\langle v_r \rangle$ maps with those in Figure 9, but for $l = 5$ data calculations. Three panels in Figure 11 show $J = 2 - 1$ transition of ^{12}CO ($y = 2 \times 10^{-4}$), ^{13}CO ($y = 2 \times 10^{-6}$), and C^{18}O ($y = 2 \times 10^{-7}$) for a viewing angle $\theta = 30^\circ$, respectively. One can observe that these maps of ^{12}CO and its isotopologue lines quite resemble each other, and they present the weak velocity gradient at the central $(2000 \text{ AU})^2$ region, of which pattern is qualitatively similar to those in Figure 9. Smaller range of $\langle v_r \rangle$ compared to SiO is either because of greater optical depth or smoother density structure in the lower resolution $l = 5$ grid data compared with the $l = 7$ data. This figure again shows that CO and isotope molecules cannot distinguish different components based on the difference in optical thickness because of the high density in the model, and puts more emphasis on the disability of CO molecules to probe embedded YPOs.

3.2.5. Position-Velocity Diagrams

We made position-velocity diagrams from the same synthesized data cubes. First we show position-velocity diagrams for $^{12}\text{CO}(2-1)$ and $\theta = 30^\circ$ in Figure 12 for $l = 7$ data for a clear view (we confirmed that $l = 5$ results are not significantly different from those of $l = 7$ calculations). All three panels in Figure 12 show almost no structure (we will discuss the origin of a spiky structure in the panel (a) below). These featureless structures in position-velocity slices can be easily inferred from the saturated shape of averaged intensity in Figure 7. In other words, velocity structures of the hydrodynamic data vanish in the structureless T_{ex} distribution and huge optical thickness even in the non-zero velocity part ($|v_r| \lesssim 2$ km s $^{-1}$). Panel (c) of Figure 12, which is a cut passing through the region about 50 AU offset

from the center, shows a similar but weaker spiky structure as in panel (a). The origin of these spikes in panels (a) and (c) is the same (see below). The cut of panel (b) passes through the center, and because of the large optical thickness, it has only a weak velocity gradient.

On the other hand, SiO lines which have much smaller optical thicknesses present a variety of structures in position-velocity diagrams due to the non-LTE energy level population (Figure 13, SiO(7 – 6) and $\theta = 30^\circ$). The most characteristic features are: 1) some of these diagrams show a “gap” around $v_r = 0 \text{ km s}^{-1}$ (panels (a), (c) and (d)), 2) a pair of cuts at the close position ($\lesssim 50 \text{ AU}$) along the same direction, such as a pair of (b) and (c), presents drastically different structures in corresponding position-velocity diagrams. A pair of (d) and (e) is another good example. These features are combination of a variety of densities (or emissivities) of the (relatively dense) outflows and the protostellar disk that have different bulk velocities. Position-velocity diagrams can be used in combination with velocity channel maps (§3.2.6) and line profiles (§3.2.7) to interpret velocity field. These variety of structures in position-velocity diagrams are obviously useful to reconstruct the original velocity and density fields from emission lines, although requires high angular resolution observation.

Finally we mention the origin of the spikes of $\Delta v_r \sim \pm 5 \text{ km s}^{-1}$ in panel (a) in Figures 12 and 13. These arise from the high velocities in the vicinity of the first core at the center and thermal broadening. Kinetic temperature in the adopted snapshot is almost isothermal of low $T_{\text{kin}} = 10 \text{ K}$, but in the limited region close to and in the first core T_{kin} rises rapidly as high as 177 K at a maximum, which corresponds to the thermal width $\Delta v_{\text{th}} \sim 2 \text{ km s}^{-1}$. In our numerical model, the magneto-centrifugal force associated with the “hour-glass” shaped magnetic fields formed around the rotating first core drives the outflow of a wide opening angle (e.g., Tomisaka 1998, 2000; Machida et al. 2008). In this model, magnetic field is straight on the z -axis (the outflow axis) and thus the magneto-centrifugal force does not work there. The velocity near the z -axis is not outward, but inward. At the center where gravitational potential depth is at its maximum, the inflow motion takes its maximum velocity as high as 1.8 km s^{-1} . The combination of a wide thermal width and the highest velocity (in the whole snapshot data) results in spikes in panel (a) in Figures 12 and 13 with a very large velocity range in the position-velocity diagrams. Because of the large thermal broadening, velocity range at these spikes becomes larger than the maximum bulk hydrodynamic velocity of the input data. To confirm the origin of these spikes, we performed line transfer experiments with the same snapshot but its kinetic temperature is set to be 10 K isothermal. The spikes disappear in these experiments, as expected.

3.2.6. Velocity Channel Maps

As an alternative expression of the velocity field imprinted in line emission, we show the velocity channel map of SiO(7 – 6) line in Figure 14. In Figure 14, extended diffuse components appearing in the velocity range $-0.6 \text{ km s}^{-1} \lesssim v_r \lesssim 0.6 \text{ km s}^{-1}$ are emission from the rotating protostellar disk. The accreting envelope extending further outside does not contribute in the channel map, since its density ($n \simeq 10^6 \text{ cm}^{-3}$) is smaller than critical density of SiO(7 – 6) ($n_{\text{crit}} \simeq 1.3 \times 10^7 \text{ cm}^{-3}$ at $T_{\text{kin}} = 10 \text{ K}$). The density in the snapshot has a cavity-like structure and a slightly denser fan-shape structure surrounding it (see Figure 1). However in the channel map (Figure 14) the fan-shape structure close to the outflow launching region is hardly observed because of the geometrically thick protostellar disk, even in the edge-on view. Only in a very limited range of velocity channels and viewing angles can we see the fan-shape structure. This fan-shape structure is due to the magneto-centrifugal force driven flow from the rotating first core, and does not come from entrainment of the core matter by a high-velocity jet. Our results mean that close attention should be paid in inferring a driving mechanism of outflows from observed channel maps especially when the target protostellar object is at the young evolutionary stage.

One of advantages of velocity channel maps is that it can demonstrate the rotational motions of the outflows more clearly compared to other diagrams. For a comparison we plot a channel map expected for the identical dataset except for $v_\phi = 0$ in Figure 15 (see §3.2.4). Comparison with Figure 14 clearly shows the existence or absence of rotation of the outflows. High angular resolution observations with the ALMA telescope will reveal these complex structures of rotating outflows coupled with a protostellar disk. Note that further imaging simulations are necessary to examine whether the diffuse emission from the protostellar disk can be correctly imaged with ALMA or other interferometers (e.g., Kurono, Morita & Kamazaki 2009). Tentative experiments showed that the total power array of the ALMA telescope is crucial to reproduce the diffuse emission in Figures 14 and 15 (Kurono & Yamada, private communication).

3.2.7. Line Profile Distributions

Finally we present an example of line profile distribution map in Figure 16 (SiO (7 – 6) of $\theta = 30^\circ$ view). Figure 16 shows that subthermal lines have double-horn or multi-peak profiles almost over the entire field-of-view. A nearly flat profile at the map center comes from a combination of large bulk velocity near the first core and a broad thermal width in the region (§3.2.5). Blue component is relatively brighter on average (Figure 8), but opposite trend (brighter red component than blue one) appears locally. This average blue-

ward skewness would largely come from the overall contraction of the core (Zhou 1995; Evans 1999).

A protostellar object at the very young evolutionary stage has a quite complicated velocity structure composed of accretion of the parent molecular core, rotation, and outflow motion and so forth. Therefore, as often referred in studies of spherical starless or prestellar cores (Pavlyuchenkov et al. 2008; Tsamis et al. 2008), the relation between emission features regarded as signatures of infall motions (e.g., blue-red asymmetry in line profiles) and actual infall motions is not necessarily well-established. For example, in our calculations, the snapshot data has an infall motion in almost entire computational domain and optical thickness large enough for self-absorption, nevertheless local enhancement of red intensity over blue is observed in some lines of sight. Adelson & Leung (1988) found that rotation and expansion motions can show a similar double-horn profile with a brighter red component compared to a blue one. Interestingly, our simulation results show double-horn profiles even in the outer part, though weak, where the optical thickness is not very large. The asymmetric double-horn profile is basically a result of combination of several factors such as: 1) blue-enhancement by asymmetric self-absorption due to the increasing T_{ex} toward the center in infall motion (Evans 1999), and 2) bipolar velocity (infall, outflow, and rotation) reflected in the optically thin regime. An additional numerical experiment is performed in order for a simple examination of emissions from different velocity components. We constructed two modified input data that have 1) radial infall velocity field outside the outflow regions ($\mathbf{v} = \mathbf{v}_r = \min(\mathbf{v} \cdot \mathbf{e}_r, 0)\mathbf{e}_r$, where \mathbf{e}_r is a unit vector in the radial direction; case A), and 2) the outflow region velocity only ($\mathbf{v} = (\mathbf{v}_{\text{out}} \cdot \mathbf{e}_z)\mathbf{e}_z$; case B). In case B, the outflow region velocity \mathbf{v}_{out} is defined as the velocity having $|v_z| > 0.5 \text{ km s}^{-1}$: this criterion turned out to be able to effectively capture the outflow region after several experiments. Figure 17 shows the results of line transfer simulation using these artificially constructed data. Panel (a) of Figure 17 shows the result of case A. It shows blue-red infall asymmetry almost over the entire field-of-view and confirms this asymmetry in Figures 8 and 16 originates in overall infall motion of the core. Panel (b) of Figure 17, on the other hand, represents almost symmetric double-horn profiles especially in the vicinity of the projected outflow axis. Since in this result the infall velocity is artificially fixed to be 0 except for that on the z -axis (see §3.2.5), this symmetric profile would come from the bimodal outflow motion itself, and the skewed profiles close to the $z = 0$ plane would be due to the protostellar disk. In the full data set simulation, these components couple nonlinearly with structured emissivity, optical thickness, and excitation temperature in different velocity and position. Further detailed analysis is necessary to disentangle them in a qualitative way.

3.3. Velocity Structure and Line Emission

As displayed in the previous subsection §3.2, line emissions from YPOs are quite complicated. In Figure 18 we plot relations between bulk velocity and local density of the adopted snapshot data in the two-dimensional probability distribution function (PDF). Figure 18 shows that: 1) distribution of v_ϕ and $|\mathbf{v}|$ with respect to density is qualitatively similar, and 2) either of $v_\phi = 0$ or $|\mathbf{v}| = 0$ components are not significant in mass. The velocity of the magneto-centrifugal force driven outflows are roughly equal to the Kepler speed (e.g., Kudoh & Shibata 1997), and then in the adopted snapshot, v_{rot} , v_{inf} and v_{out} (rotation, infall and outflow speeds) become comparable. Hence the first feature in Figure 18, similarity in the distributions of v_ϕ and $|\mathbf{v}|$, represents comparable speed of v_{rot} , v_{inf} and v_{out} . Taking into account the symmetric structure of the input snapshot with respect to the $z = 0$ plane and the geometrically thick configuration of the protostellar disk, it explains a complex velocity structure that multiple velocity components with similar norms but different signs easily appear in the field-of-view (or on a line-of-sight) whichever inclination angle aligns the object. In a more evolved object such as seen in current observations, the velocity structure becomes simpler mainly because a protostellar disk will evolve to a thinner rotationally supported circumstellar disk with relatively small spatial extent compared to the outflows. Hence a complex velocity feature is a manifestation of dynamical evolution of the star-forming object in the young evolutionary stage, when the outflows are embedded in the accreting envelope and the thick protostellar disk. Therefore such complexity in emission induced by complex velocity structure is a characteristic of the early stage of star formation.

We plot the relation between bulk velocity of the snapshot data and excitation temperature obtained in line transfer calculations in Figure 19 for SiO(2 – 1) and (7 – 6) lines as two-dimensional PDFs. Figure 19 shows that T_{ex} has a wide scatter as a function of velocity, and hence self-absorption will be possible at various velocities. Particularly, a relatively large scatter of T_{ex} around $v_\phi = 0$ and $v_z = 0$ suggests a large possibility of self-absorption at zero velocity as well. Either a small amount of matter with $\mathbf{v} = 0$ (Figure 18) and high probability of self-absorption at $v_\phi = 0$ or $v_z = 0$ (Figure 19) can weaken the line emission at $v_r = 0$ compared to the other velocity components. This causes the gap at $v_r = 0$ in position-velocity diagrams in Figure 13. The gap structure in position-velocity diagram were already seen in observation (e.g. Hogerheijde et al. 1998; Williams et al. 2003; Lee et al. 2006). On the other hand, energy level population of ^{12}CO is almost fully thermalized in the nearly isothermal snapshot, thus $T_{\text{ex}} \simeq T_{\text{kin}} \simeq 10\text{K}$ and ^{12}CO lines do not show a gap in position-velocity diagram (Figure 12). Since neither Figures 18 nor 19 include spatial correlation, they cannot explain all the features of emitted lines. All the arguments above are statistical. Further detailed analysis of spatial structures will appear in the following article.

4. Discussion

The early phase of protostellar objects and their evolution in its beginning are quite interesting and important problems in the study of star formation. For the formation of low-mass stars, a model of Adams, Lada & Shu (1987) of spectrally categorized young stellar objects from Class 1 to Class 3 has been widely accepted. While multi-dimensional studies using numerical methods have constructed realistic evolutionary models of molecular cores to protostars (see e.g., Tomisaka 1998, 2000, 2002; Banerjee & Pudritz 2006; Machida et al. 2006, 2008; Hennebelle & Fromang 2008), observational studies have proceeded on the basis of classical spherical models. One of the difficulties in observational studies of the early stage of star formation is its deeply embedded signature in the parent molecular core. Observations have found a numbers of non-radial velocity fields in mostly spherical molecular cores (e.g., Belloche et al. 2002), but they have been interpreted in terms of a simple superposition of arbitrarily introduced rotation or outflow/inflow motions within the framework of classical spherical models. High angular resolution observation facilities like the ALMA telescope are expected to provide information of velocity fields even in small structures within a protostellar object. However, as shown in the previous sections, the signals of emission from a YPO deeply embedded in the envelope are difficult to correctly decipher even with the high angular resolution of the ALMA telescope, because of the complex velocity field and resultant complicated optical thickness structure. Furthermore identification of outflow itself would be far more difficult compared to the case of more evolved outflows currently observed (Figure 14). Therefore, careful investigation of how the true structures of objects are reflected in emission from them is necessary.

Recently the *Spitzer Space Telescope* found numbers of very low luminosity objects (VeLLOs) in the mid-infrared band. The distribution of molecular gas accompanying these objects and the existence or absence of outflow are quite uncertain (Bourke et al. 2006; Yamada & Ohashi, private communication). If these VeLLOs are indeed related to the very early phase of star formation, irregular morphology of molecular emission might also be a natural consequence (e.g., Figure 14). If future high-angular resolution observation of molecular emission of VeLLOs indicates an outflow signature, comparison of our results would provide a valuable insight on the earliest phase of star formation. Among VeLLOs, for example, a molecular core L1521F in Taurus has a high central density, infall asymmetry, and is chemically evolved. Since the discovery of a weak infrared source by the Spitzer telescope, it is considered to be an object on the evolutionary way from an evolved starless core and Class 0 protostar stage (Bourke et al. 2006), thus it would be a good candidate to be studied in the future high-angular resolution observation with the ALMA telescope to test the prediction of our paper. A more evolved VeLLO, IRAM 04191+1522 also in Taurus will be another good target of the ALMA telescope in the study of the early stage of star

formation. Besides VeLLOs, it might be possible that rotation signatures like Figure 14 were considered to be a manifest of other kinds of velocities in some of the observation of irregular outflows in young YSOs (see e.g., Di Francesco et al. 2001).

4.1. Relevant Radiative Transfer Simulation Studies

Recently line transfer simulation studies of star formation have increased in number. Many works on the early phase of star formation focus on chemical evolution in their one-dimensional modelling rather than on dynamical evolution. Tsamis et al. (2008) employed the inside-out collapse solution of Shu (1977) and calculated chemical evolution along with line transfer in collapsing cores. They constructed a virtual 45-m class telescope and performed pseudo-observation of their simulation results. Pavlyuchenkov et al. (2008) systematically examined the effects of rotation and infall motions on emergent line emission with their one-dimensional modelling. Complex velocity fields (infall, rotation and outflow) in the early protostellar objects affect the emission line profiles in a quite non-trivial way (§3.2.7). Generally blue-skewed asymmetry and inverse P-Cygni profiles are regarded to evidence an infall motion as well-understood mechanisms. However, quantitative understandings of the effects of gas motion on line emission is not significantly well developed to solve an inverse problem. In other words, we currently still cannot reconstruct the velocity field from the obtained line profiles to a satisfactory degree for a comparison with theoretical models, even for a spherical gas. These works are experimental rather than applicable for asymmetric objects in real space, nevertheless they will form a powerful set of building blocks in interpreting more realistic simulation results like ours and observational results.

Many numerical works have been done in order to derive physical quantities of outflows in observation data so that models can fit the observational results. Meyers-Rice & Lada (1991) performed numerical experiments of a simple concave model outflow, and Rawlings et al. (2004) succeeded in constructing a best fit structure to the results of Hogerheijde et al. (1998), that consists of outflow cones and a surrounding envelope with their two-dimensional radiative transfer calculations. These studies employed minimal models to reproduce the temporal structure imprinted in observations. On the other hand, in more realistic calculations presented in this article, the most difficult factor in the identification of the emission components from the outflows is the contamination from the geometrically and optically thick protostellar disk (Figure 14). In a more evolved system, outflows cover wider spatial extents than the protostellar disk, and the protostellar disk will evolve to a flatter circumstellar disk, so that the outflows are observable without shielding of a thick disk. In other words, the youngest outflows would not appear similar to those seen in current observation. Inter-

ferometric observational studies proposed a disk/outflow model based on multi-components appearing in their data, but with an assumed geometrically thin disk. Possible effects on the emission by a thick protostellar disk on the evolution toward a circumstellar disk is first mentioned in this article. A thick protostellar disk appears in a number of numerical studies (Tomisaka 1998, 2000, 2002; Banerjee & Pudritz 2006; Machida et al. 2006, 2008). Detailed study of emission is necessary for a verification of these results in future observations.

4.2. Launch of Outflows

Our calculations have a relation to outflow launching mechanisms. One of the characteristic features of outflows driven by magneto-centrifugal force is its rotation around the flow axis. In contrast, if the outflow is accelerated by the momentum transfer from the jet (so-called “entrainment” mechanism), the molecular outflow would rotate very slowly. This is expected by the fact that, in the entrainment mechanism, the angular momentum is not effectively redistributed from the jet which has a small angular momentum to the molecular outflow which has a large moment of inertia. Our line transfer calculations have shown that the rotation of the outflows appears in velocity channel maps, position-velocity diagrams and maps of $\langle v_r \rangle$. Launhardt et al. (2009) recently found a gradient of $\langle v_r \rangle$ supposed to present rotation of an outflow from a transition object from Class 1 to Class 2 (or younger), CB 26 in their IRAM PdBI observation. In addition to an evolved system like CB 26, if rotation of outflows in younger objects will be discovered, they will be a good constraint for the models of outflow launching mechanisms. The younger the object, the tighter the constraint will be, though a younger system is embedded in an envelope of parent molecular core matter, and its definite detection is more difficult. We found a signature from rotation of the outflows in velocity channel map, position-velocity diagrams and distribution of $\langle v_r \rangle$. Further analysis of the line profile distribution as well as those in Figure 17 will provide clearer indications of the rotation signatures, and will appear in a future article.

In the evolution model we employed in this article (Tomisaka 1998, 2000, 2002; Machida et al. 2008), outflows are driven just outside a first core. The strongest support for their model will then come from the emission from the first core. However, we cannot derive any strong conclusion about this, since the numerical modeling adopted in this article cannot resolve a geometrically thin shocked region at the surface of the first core, and cannot follow the shock chemistry inside such a thin region. Omukai (2007) and Saigo & Tomisaka (2009) calculated emission from a thin cooling shock surrounding a first core. They consistently examined emission from the radiative shock and absorption/re-emission in the surrounding envelope by sacrificing the detailed dynamical evolution. Omukai (2007) found that reprocessings

in the thick envelope is significant in a spherical cloud, whereas Saigo & Tomisaka (2009) showed that rotation flattens the cloud and reduces the column density along the rotation axis by more than one order of magnitude. Our three-dimensional calculations of longer wavelength emission, mainly for the ALMA telescope, showed that line emission can be seen through the wider velocity range due to the non-spherical motions and geometry. Different from Omukai (2007) and Saigo & Tomisaka (2009), our calculations do not explicitly include an outer absorbing envelope (§2.2). Though we conclude that the outer envelope would not qualitatively alter our results of SiO lines of $l = 7$ grid by a simple survey of line profiles in $l = 5$ calculation, these effects in outer envelope absorption and optical thickness should be included in an advanced numerical scheme in the future.

4.3. Comments on the Real Observations

Finally we briefly comment on the real observations especially with the ALMA telescope. Our calculations are the appropriate means for comparing the results of MHD calculations with observations since we calculate the radiation explicitly. This article focuses on the study of characteristic features of radiation field of a YPO, and does not include any limitations from observational instruments such as finite beam size (compare with e.g., Tsamis et al. 2008). Although our results are ideal, we can make a simple estimate of the necessary observation time by the ALMA telescope using the synthesized emission presented in this article. If we assume a YPO at the distance of 140 pc and declination $\delta = -30^\circ$, typical size of the characteristic features in the synthesized maps (Figures 5, 6, 14 and 15) is $\gtrsim 10$ AU, or $\sim 0.1''$ in angular size. From Figure 8, the brightness temperature of SiO(7–6) line is ~ 3 K, and line width is ~ 2 km s $^{-1}$. Then if we invoke the velocity resolution to be 0.1 km s $^{-1}$, which is used in our calculation, and 0.3 K sensitivity, the necessary exposure time amounts to ~ 5100 seconds or ~ 14 hours. For the continuum, the required exposure time reduces to ~ 2.6 hours for the same object but 2 mK sensitivity because of a large bandwidth of the receivers installed on the ALMA telescope (§3.1). It is noted that one should be careful whether diffuse emission from the protostellar disk in Figures 14 and 15 can be correctly reproduced in interferometer observations or not. The tentative results of such imaging simulation for the ALMA telescope suggest that in order to reproduce the diffuse component, the total power array is crucially important, and the above estimates assume the use of the full array (12 m, 7 m, and the total power array; Kurono & Yamada, private communication). Lower J lines, of which critical densities are lower than the average density in the protostellar disk and the envelope, appear even extended than Figure 14. Besides the limitation that comes from radiative transfer scheme (§2.2), imaging simulation for interferometers will be necessary for direct comparison of our results with actual observations (Takakuwa et al. 2008;

Kurono et al. 2009).

5. Summary

In this article we surveyed the characteristic features of the radiation field from a dynamically evolving object at an early stage of star formation, on the way from a prestellar (starless) core to a Class 0 object. We have presented the most realistic calculation results obtained to date from a combination of three-dimensional MHD simulation and non-LTE line transfer calculations. We calculated the dust thermal emission and rotational lines of ^{12}CO (and its isotopic molecules) and SiO molecules in the snapshot data consisting of the compact outflows ($R \sim 1000$ AU), the protostellar disk and the envelope. We found that:

1) Dust thermal emission traces a dense mid-plane in the protostellar disk rather than very small structures in the launching region of the outflows. A very weak fan-shape signature along the base of the outflows appears in viewing angles close to edge-on, but it is likely to be overwhelmed by the much brighter protostellar disk.

2) Because of the high density ($n \gtrsim 10^6 \text{ cm}^{-3}$) in our snapshot data, ^{12}CO and its isotopologue lines are fully thermalized and are not suitable to probe velocity field. Our results are in apparent disagreement with current observation of more evolved outflows, but can be reasonably understood in terms of the different densities at different evolutionary stages. This implies that the energy level population of CO is governed by collisional transitions, and the molecular abundance does not significantly affect the results. We experimented with lower molecular abundances to mimic possible depletion of ^{12}CO molecules, and found no significant differences in the final results.

3) On the other hand, SiO lines are not completely thermalized because of their higher critical densities ($n_{\text{crit}} \sim 10^5 \times J^3 \text{ cm}^{-3}$), and are more suitable for probing the velocity structure in contrast to CO. Line profiles of SiO are characterized by a double-horn shape over almost the entire field-of-view, and position-velocity diagrams showed a variety of structures strongly dependent on locations of different cuts. These structures arise from a complex distribution of optical thickness and non-LTE energy level populations induced by several velocity components, such as outflow, inflow, and rotation. In a dynamically evolving system, these velocity components have similar speeds but different directions, thus any line-of-sight can pick up multiple velocity components of similar norms but different signs irrespective of viewing angles. In order for a correct interpretation of such complex velocities from line emission, further detailed analysis is necessary.

4) In the adopted model in this article, the outflows are driven by a magneto-centrifugal

force (Machida et al. 2006, 2008). One of the characteristics in magneto-centrifugal force driven flows is their rotation around the axis. Its signature can appear in intensity-weighted velocity maps and velocity channel maps of the synthesized radiation, and should be observable with the ALMA telescope with a reasonable time (~ 14 hrs for SiO(7 – 6) line and ~ 2.6 hrs for continuum at 350 GHz). Several models have been proposed for launching mechanism of molecular outflows (see e.g., Arce et al. 2007), but are still in dispute. Our results showed a clue to identify the signature of magneto-centrifugal force driven models (rotation of the outflows: Figure 14), and will be an important step towards understanding of the early stage of star formation.

Based on the limitation of the outer boundary for the radiative transfer calculations, our results should be taken as rather qualitative, and not quantitative for comparison to real observations. Further studies will be needed for a confronting theoretical model prediction for the ALMA telescope and for revealing, in particular, the connection between velocity and emission lines.

We thank T. Matsumoto and T. Hanawa for contribution to the nested grid code used in hydrodynamic simulation. M.Y. thanks for intriguing and inspiring discussion and comments of N. Hirano, C.-F. Lee, N. Ohashi and M. Momose, and R. Taam for his critical reading of this article. Numerical computations were partly carried out on VPP5000 and Cray XT4 at the Center for Computational Astrophysics (CfCA), National Astronomical Observatory of Japan, and this research was supported in part by Grants-in-Aid by the Ministry of Education, Science, and Culture of Japan (17340059, 16204012, 18740104).

REFERENCES

- Adams, F. C., Lada, C. J. & Shu, F. H. 1987, *ApJ*, 312, 788.
- Adelson, L. M. & Leung, C.-M. 1988, *MNRAS*, 235, 349.
- Aikawa, Y., Ohashi, N., Inutsuka, S., Herbst, E. & Takakuwa, S. 2001, *ApJ*, 522, 639.
- André, P., Motte, F., & Bacmann, A. 1999, *ApJ*, 513, L57.
- Arce, H. G., et al. 2007, *Protostars and Planets V*, Reipurth, B., Jewitt, D. & Keil, K. (eds.), University of Arizona Press, Tuscon, 951, 245.
- Banerjee, R. & Pudritz, R. E. 2006, *ApJ*, 641, 949.
- Beckwith, S. V., Sargent, A. I., Chini, R. S. & Güsten, R. 1990, *AJ*, 99, 924.

- Belloche, A., André, P., Despois, D. & Blinder, S. 2002, *A&A*, 393, 927.
- Bourke, T. L. et al. 2005, *ApJ*, 633, L129.
- Bourke, T. L. et al. 2006, *ApJ*, 649, L37.
- Caselli, P., Hartquist, T. W., & Havens, O. 1997, *A&A*, 322, 296.
- Caselli, P., Benson, P. J., Myers, P. C., & Tafalla, M. 2002, *ApJ*, 572, 238.
- Codella, C., Bachiller, R. & Reipurth, B. 1999, *A&A*, 343, 585.
- Di Francesco, J., Myers, P. C., Wilner, D. J., Ohashi, N. & Mardones, D. 2001, *ApJ*, 562, 770.
- Dunham, M. M. et al. 2006, *ApJ*, 651, 945.
- Evans, N. J. II, 1999, *ARA&A*, 37, 311.
- Flower, D. R., Pineau des Forêts, G., Walmsley, C. M. 2005, *A&A*, 436, 933.
- Gibb, A. G., Richer, J. S., Chandler, C. J., & Davis C. J. 2004, *ApJ*, 603, 198.
- Goodman, A. A., Barranco, J. A., Wilner, D. J., & Heyer, M. H. 1998, *ApJ*, 504, 223.
- Hennebelle, P. & Fromang, S. 2008, *A&A*, 477, 9.
- Hildebrand, R. H. 1983, *Royal Atron. Soc. Quart. Jrn.* 24, 267.
- Hirano, N. et al. 2006, *ApJ*, 636, L141.
- Hogerheijde, M. R., van Dishoeck, E. F., Blake, G. A., & van Langevelde H. J., 1998, *ApJ*, 502, 315.
- Hogerheijde, M. R., & van der Tak, F. F. S. 2000, *A&A*, 362, 697.
- Jørgensen, J. K., Schöier, F. L., & van Dishoeck, E. F. 2005, *A&A*, 435, 177.
- Jørgensen, J. K., Johnstone, D., van Dishoeck, E. F., & Doty, S. D. 2006, *A&A*, 449, 609.
- Kudoh, T. & Shibata, K. 1997, *ApJ*, 474, 362.
- Kurono, Y., Morita, K. & Kamazaki, T. 2009, accepted for publication in *PASJ*.
- Langer, W. D., & Glassgold, A. E. 1990, *ApJ*. 352, 123.
- Larson, R. B. 1969, *MNRAS*, 145, 271.

- Launhardt, R. et al. 2009, *A&A*, 494, 197.
- Lee, C. -F. et al. 2006, *ApJ*, 639, 2006.
- Machida, M. N., Matsumoto, T., Hanawa, T. & Tomisaka, K. 2005, *MNRAS*, 362, 382.
- Machida, M. N., Inutsuka, S. & Matsumoto, T. 2006, *ApJ*, 647, L151.
- Machida, M. N., Inutsuka, S. & Matsumoto, T. 2008, *ApJ*, 676, 1088.
- Masunaga, H., & Inutsuka, S. 2000, *ApJ*, 531, 350.
- Matthews, B. C., Hogerheijde, M. & Bergin, E. 2006, *ASP Conf. Series*, 356, 266.
- Meyers-Rice, B. A. & Lada, C. J. 1991, *ApJ*, 368, 445.
- Myers, P. C. 1983, *ApJ*, 270, 105.
- Omukai, K. 2007, *PASJ*, 59, 589.
- Onishi, T., Mizuno, A., & Fukui, Y. 1999, *PASJ*, 51, 257.
- Pavlyuchenkov, Ya., et al. 2008, *ApJ*, 689, 335.
- Rawings, J. M. C., Pedman M. P., Keto, E. & Williams, D. A. 2004, *MNRAS*, 351, 1054.
- Saigo, K. & Tomisaka, K. 2009, in prep.
- Schilke, P., Warmley, C. M., Pneau des Forêts, G. & Flower, D. R. 1997, *A&A*, 321, 293.
- Schöier, F. L., van der Tak, F. F. S., van Dishoeck, E. F. & Black, J. H. 2005, *A&A*, 432, 369.
- Shu, F. H. 1977, *ApJ*, 214, 488.
- Takakuwa, S. et al. 2007, *PASJ*, 59, 1.
- Takakuwa, S. et al. 2008, *ApSS*, 313, 169.
- Tomisaka, K. 1998, *ApJ*, 502, L163.
- Tomisaka, K. 2000, *ApJ*, 528, L41.
- Tomisaka, K. 2002, *ApJ*, 575, 306.
- Truelove, J. K., Klein, R. I., McKee, C. F., Hlliman, J. H., Howell, L. H. & Greenough, J. A. 1997, *ApJ*, L179.

- Tsamis, Y. G., Rawlings, J. A., Yates, J. A. & Viti, S. 2008, MNRAS, 388, 898.
- van der Tak, F. et al. 2005, proceedings of “Dusty and Molecular Universe : a Prelude to Herschel and ALMA”, ed. by Wilson, A. 431.
- Wada, K. & Tomisaka, K. 2005, ApJ, 619, 93.
- Williams, J.P., Plambeck, R. L. & Heyer, M. H. 2003, ApJ, 591. 1025.
- Yamada, M., Wada, K. & Tomisaka, 2007, ApJ, 671, 73.
- Yamada, M. & Tomisaka, K. 2009, submitted to ApJ.
- Zhou, S. 1995, ApJ, 442, 685.

Table 1: Mean optical thickness of dust emission averaged over a field-of-view $\langle\tau_\nu\rangle$ and the maximum optical thickness in the field-of-view $\tau_{\nu,\max}$ for $\theta = 30^\circ$ view. Values in this table do not strongly depend on θ (see Figure 3). Three cases with different power-law indices of opacity $\beta = 2, 1.5,$ and 1 (Eq.[9]) are listed.

ν [GHz]		150	220	350	650	850
$\beta = 2.0$	$\tau_{\nu,\max}$	0.37	0.79	2.01	6.94	11.9
	$\langle\tau_\nu\rangle$	4.31×10^{-4}	9.28×10^{-4}	2.34×10^{-3}	8.10×10^{-3}	0.0138
$\beta = 1.5$	$\tau_{\nu,\max}$	1.04	1.86	3.72	9.42	14.1
	$\langle\tau_\nu\rangle$	1.22×10^{-3}	2.17×10^{-3}	4.35×10^{-3}	0.0110	0.0164
$\beta = 1.0$	$\tau_{\nu,\max}$	2.95	4.33	6.89	12.8	16.7
	$\langle\tau_\nu\rangle$	3.45×10^{-3}	5.06×10^{-3}	8.04×10^{-3}	0.0149	0.0195

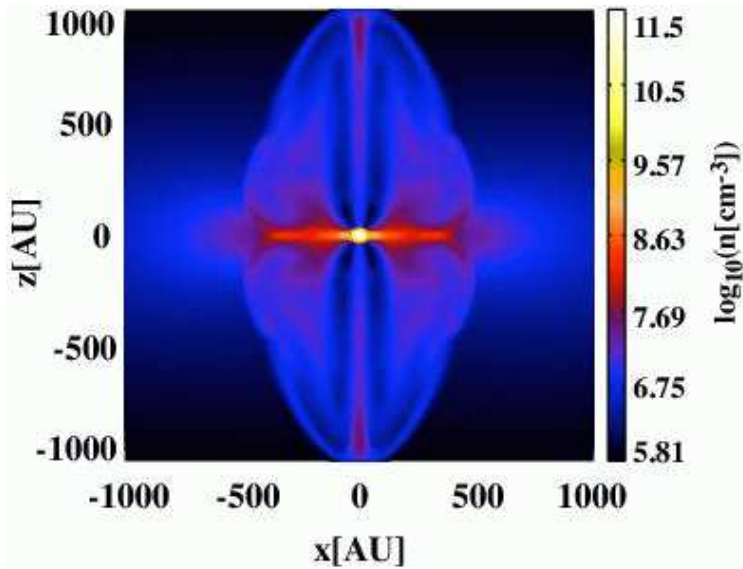


Fig. 1.— Density structure of the snapshot data used in radiative transfer simulation. The density at $x - z$ plane at $y = 0$ is displayed. Bipolar outflows extend along the z -axis ($R \lesssim 1000 \text{ AU}$), and the first core is seen as a quite compact dense region ($R \lesssim 100 \text{ AU}$) at the center. Additionally a geometrically-thick protostellar disk appears as an extended region with a scale height $\approx 200 - 300 \text{ AU}$. In the vicinity of the launching regions of the outflows, the density structure shows a cavity surrounding the central axis along the z -axis, and a shell-like dense regions of the shape of a letter “U” surrounding them.

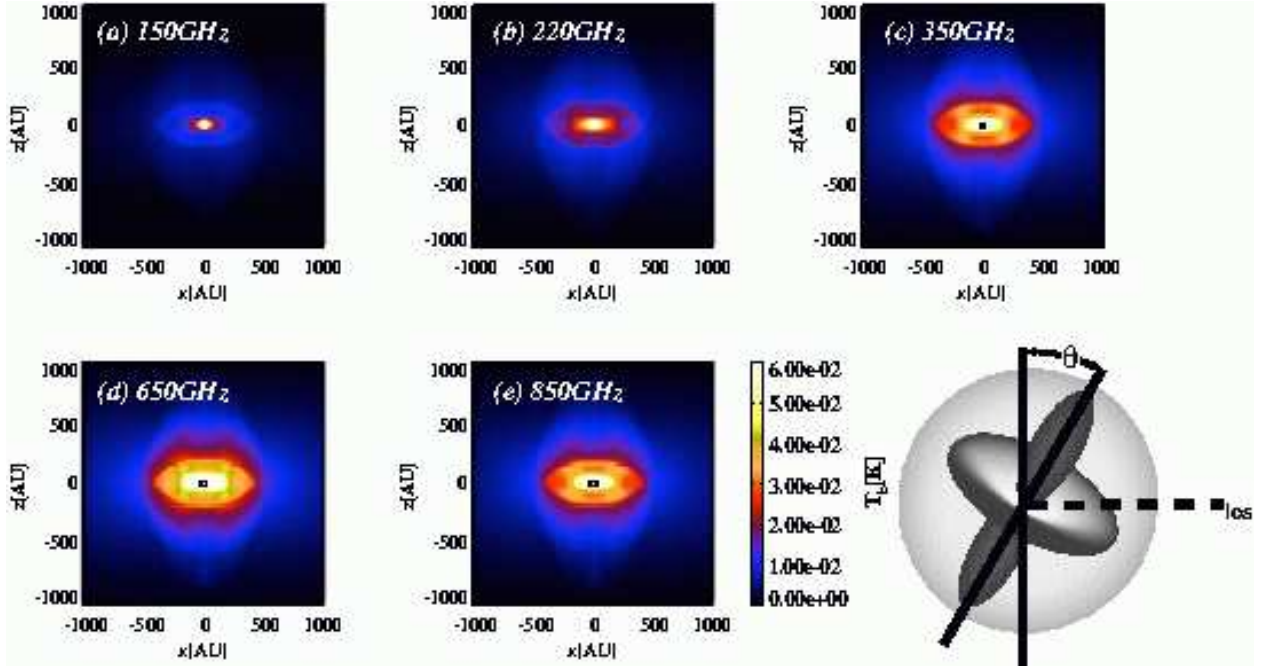


Fig. 2.— Maps of thermal emission from $T_d = 10$ K dust grains. Five panels correspond to different wavelengths in the millimeter and submillimeter bands. All these maps have an inclination angle $\theta = 30^\circ$ (see the bottom right illustration for definition of the inclination angle θ). Black solid lines at the center ($R \sim 20 - 100$ AU) of the panels (c), (d) and (e) indicate regions of which optical thickness exceeds 1. Correction of finite optical thickness for conversion from T_b to column density seems unimportant except for an innermost region even in the highest frequency in the submillimeter band in our simulation, but thick regions broaden their areas if the outer part of the simulation domain is included.

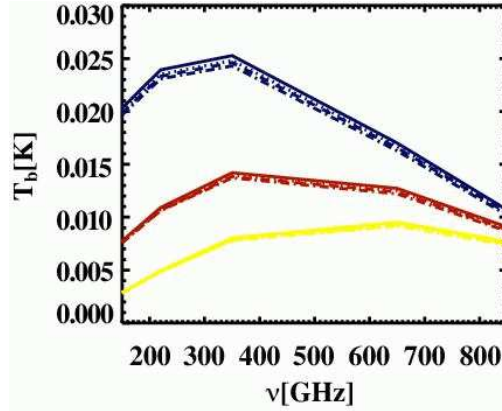


Fig. 3.— SED averaged over the field-of-view defined in the computation domain. Blue lines are for $\beta = 2$, red lines are $\beta = 1.5$, and yellow lines are $\beta = 1$, respectively. For a value of β , solid line indicates the viewing angle of $\theta = 90^\circ$ (pole-on view), dotted line is for $\theta = 60^\circ$, dashed line is for $\theta = 30^\circ$, and a dot-dashed line is for $\theta = 0^\circ$ (edge-on view).

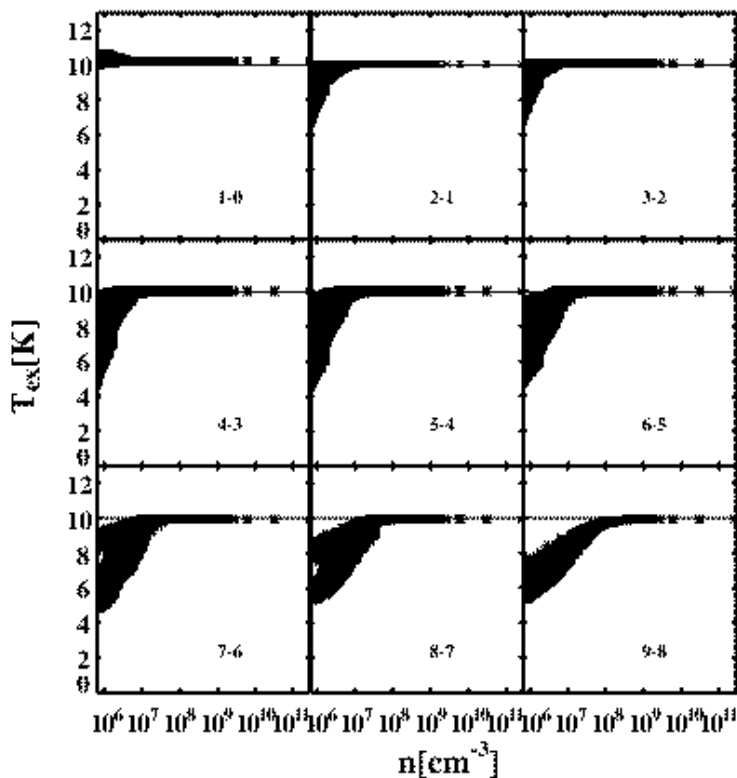


Fig. 4.— Excitation temperature of SiO line in each cell is plotted as a function of density of the cell. Thin horizontal lines at $T_{\text{ex}} = 10$ K indicate a reference for thermalization in an isothermal gas of T_{kin} of 10K. Low excitation transitions in millimeter bands ($J = 1-0, 2-1$) are almost fully thermalized, but the excitation conditions of high excitation transitions of which critical density for LTE rapidly increases with J ($n_{\text{crit}} \approx 10^5 \times J^3 \text{ cm}^{-3}$), depart from LTE in the low density regime ($n \lesssim 10^7 - 10^8 \text{ cm}^{-3}$).

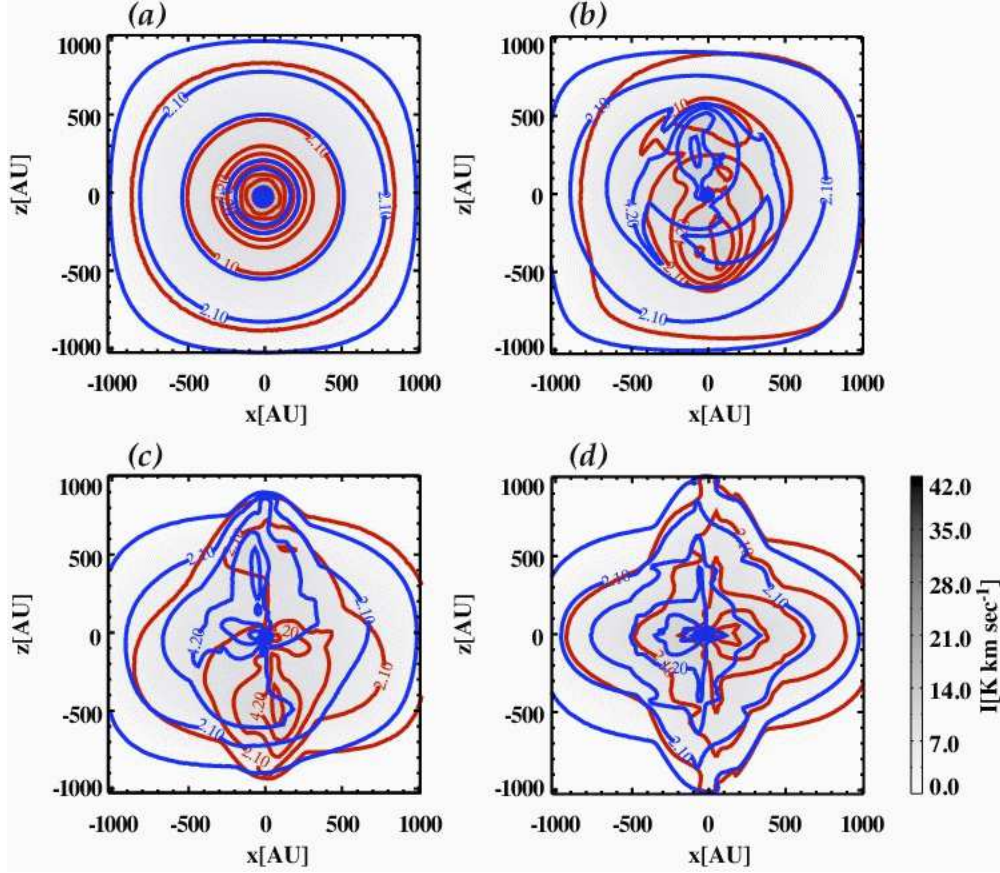


Fig. 5.— Maps of integrated intensity of SiO(7–6) line (gray scale). Four panels correspond to different viewing angles: panel (a) is $\theta = 90^\circ$, (b) is $\theta = 60^\circ$, (c) is $\theta = 30^\circ$, and (d) is $\theta = 0^\circ$. Red and blue contours indicates integrated intensities in $v_r > 0$ (red) and $v_r < 0$ (blue) components, respectively, with equal contour spacing of 1.05 K km s^{-1} .

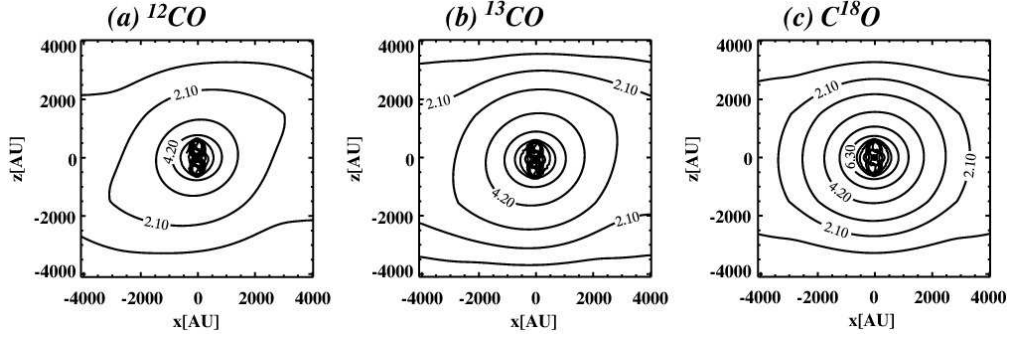


Fig. 6.— Maps of integrated intensity of ^{12}CO , ^{13}CO , and C^{18}O ($1-0$) lines taken from the $l = 5$ data calculations. Because of the use of $l = 5$ grid data, the area of the field-of-view is 16 times larger than that in Figure 5. Contours are drawn with equal spacing of 1.05 K km s^{-1} .

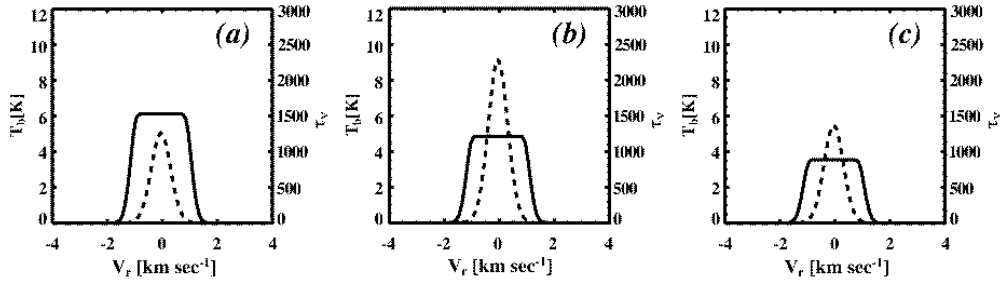


Fig. 7.— Line profiles of ^{12}CO averaged over the field-of-view (solid lines) and average τ_ν profile (dashed lines) as a function of line-of-sight velocity for $\theta = 60^\circ$ view for $l = 5$ grid. Panels (a), (b), and (c) are for different transitions, $J = 1-0$, $2-1$, and $3-2$, respectively. Because of the huge optical thickness, line profiles take a strongly saturated profile with very weak wing signatures ($|v_r| \lesssim 2 \text{ km s}^{-1}$).

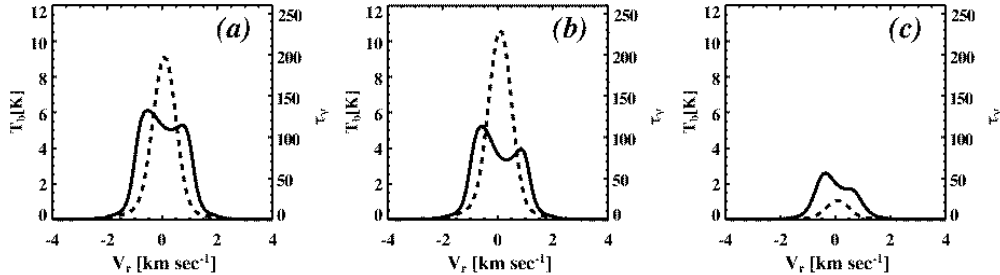


Fig. 8.— The same figures as Figure 7, but for SiO . Panels (a), (b), and (c) denote $J = 2-1$, $4-3$, and $7-6$ transitions, respectively. Mean optical thickness reduces by a factor of ~ 100 compared to ^{12}CO , and line profiles take a double-horn shape skewed to the blue side.

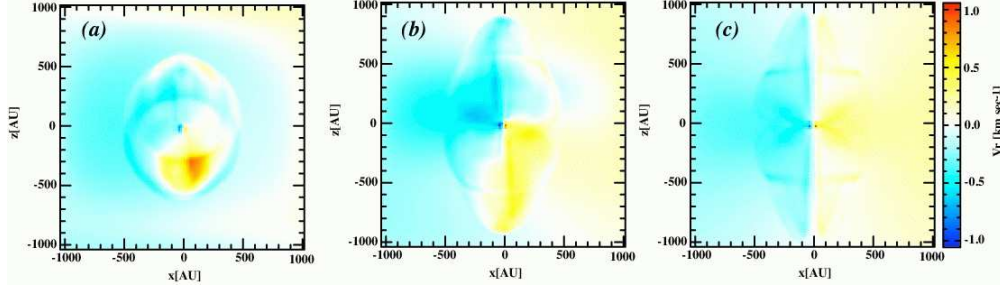


Fig. 9.— The velocity first moment ($\langle v_r \rangle$) maps of SiO(7 – 6) line. Panels (a), (b), and (c) are different inclination angles ($\theta = 60^\circ$, 30° , and 0° , respectively).

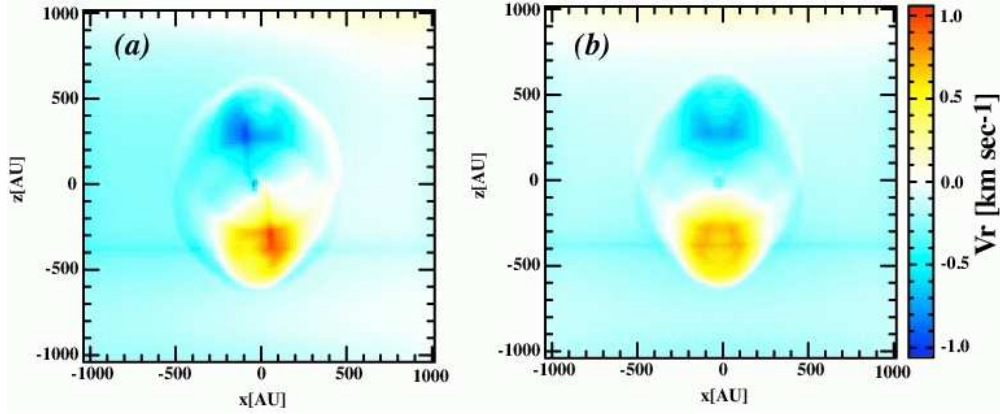


Fig. 10.— The velocity first moment $\langle v_r \rangle$ maps of SiO(4 – 3) line for $\theta = 30^\circ$ view. Panel (a) is taken from the original result with $v_\phi \neq 0$, and panel (b) is a result of $v_\phi = 0$ experiments. Symmetric and anti-symmetric distributions of peaks are due to rotation of the outflows and the protostellar disk. Similar trend is observed in all the lines we calculated.

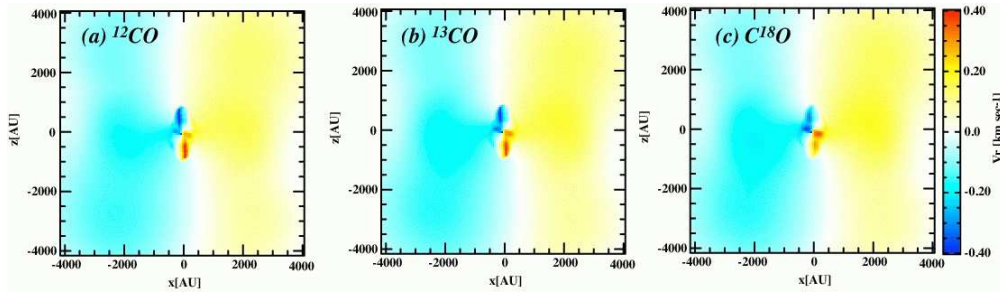


Fig. 11.— The velocity first moment ($\langle v_r \rangle$) maps of $^{12}\text{CO}(3 - 2)$ and its isotopologue line for $l = 5$ calculations. Panels (a), (b), and (c) are $^{12}\text{CO}(3 - 2)$, $^{13}\text{CO}(3 - 2)$, and C^{18}O , respectively, and have the same viewing angle $\theta = 60^\circ$. The global symmetric gradient of $\langle v_r \rangle$ would originate in the rotation of the parent core.

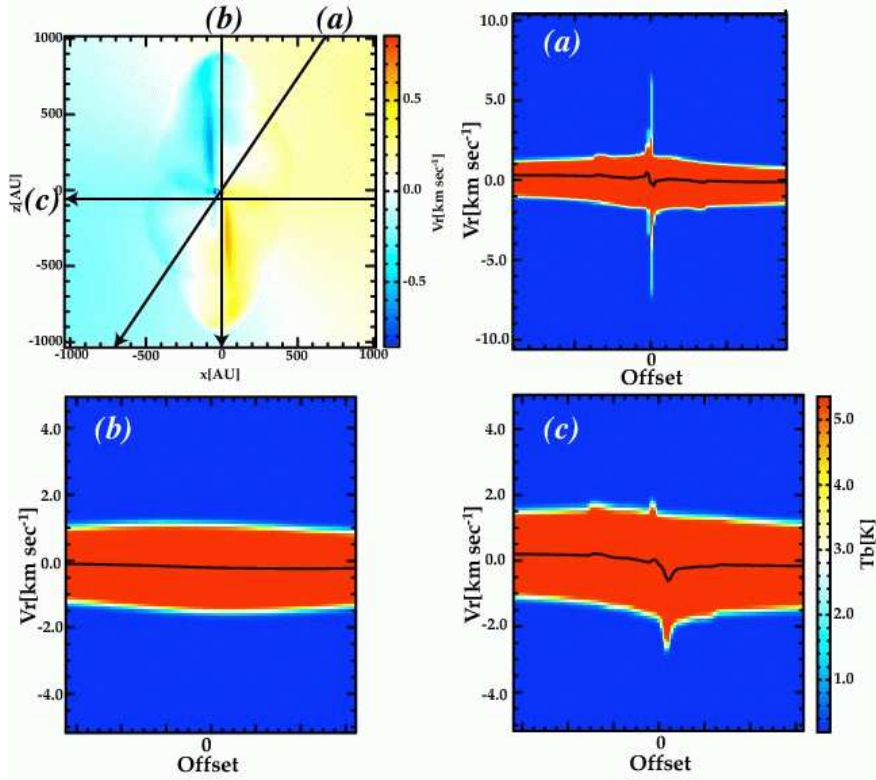


Fig. 12.— Position-velocity diagrams of $^{12}\text{CO}(2-1)$ line along three cuts indicated on the top-left panel ($\langle v_r \rangle$) for $\theta = 30^\circ$ view (data are taken from $l = 7$ grid calculation for a clear view). Width of position-velocity diagrams are scaled to the length of the cuts from the center. Solid lines indicate $\langle v_r \rangle$ along each cut.

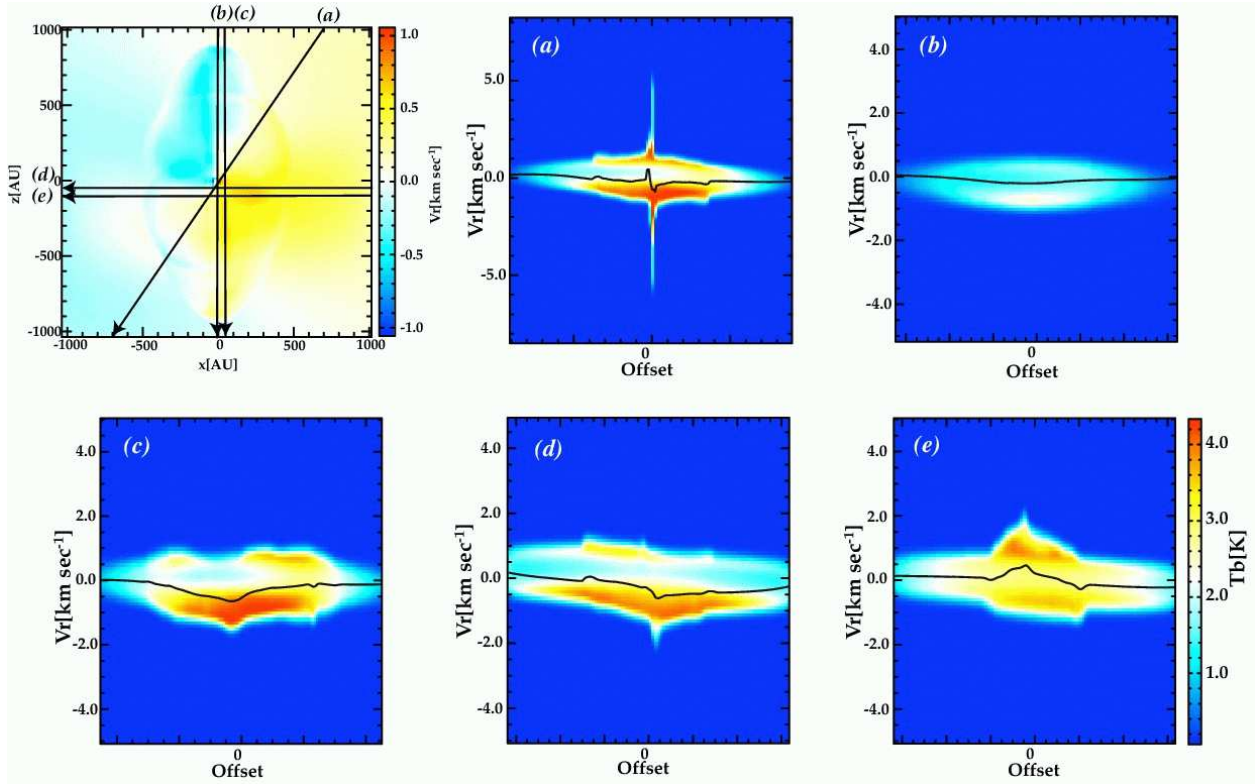


Fig. 13.— Position-velocity diagrams of SiO(7 – 6) line. Horizontal width of diagrams are similarly scaled with the cut length on the $\langle v_r \rangle$ map at the top-left. Compared with Figure 12, SiO line shows a variety of structures in these position-velocity diagrams due to the non-LTE population.

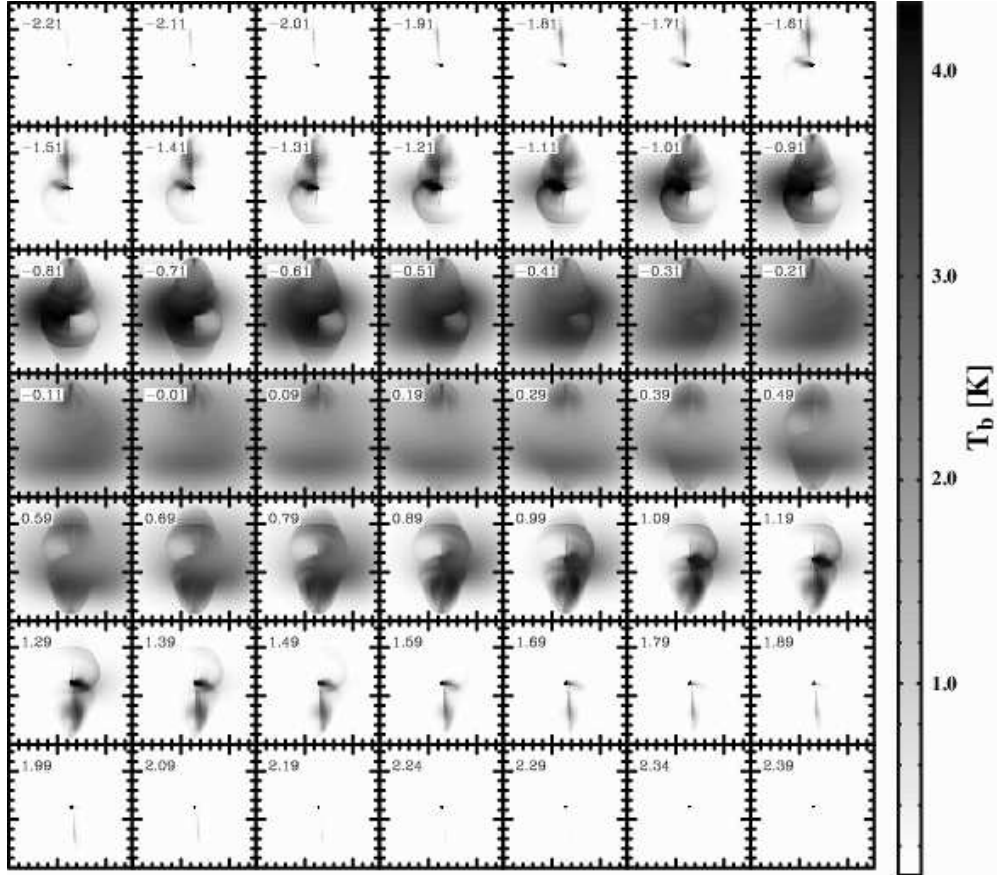


Fig. 14.— Velocity channel map of SiO(7 – 6) line for $\theta = 30^\circ$ view. The relative velocity in unit of km s^{-1} from the rest of the object is labeled at the top-left of each map. Diffuse components appearing in $|v_r| \lesssim 0.6 \text{ km s}^{-1}$ are emission from the protostellar disk. Rotation of the outflows and the protostellar disk is clearly observed.

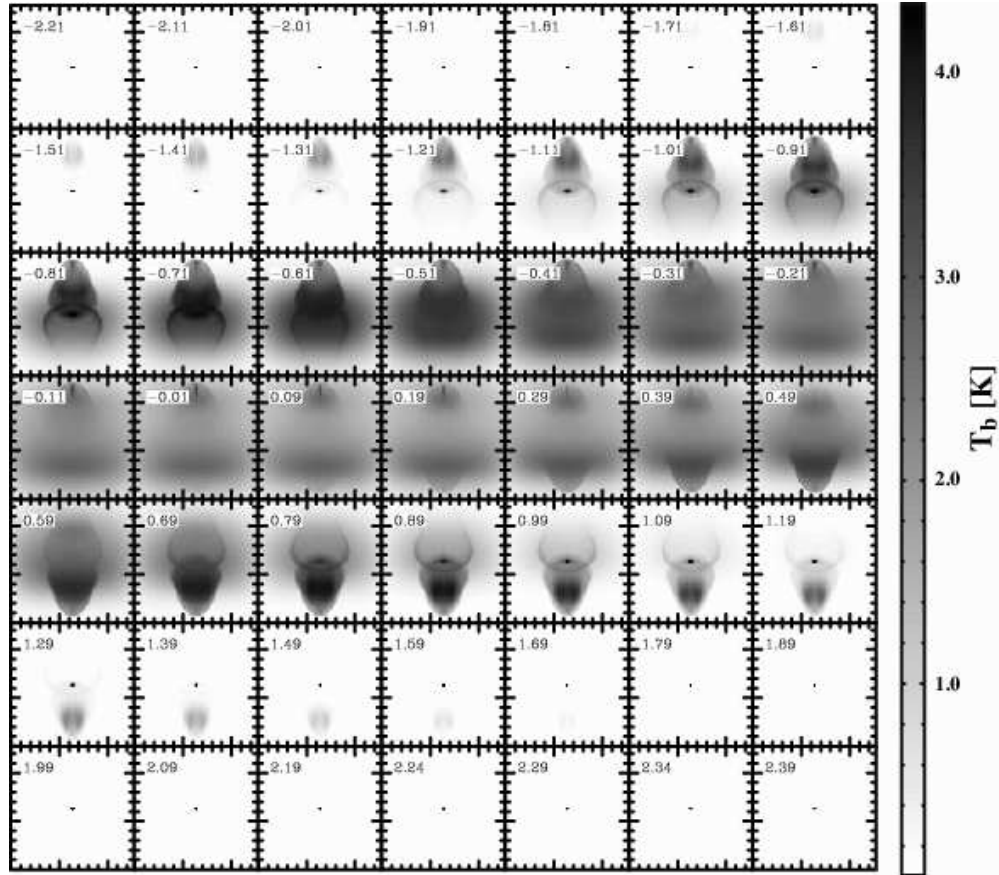


Fig. 15.— Same as Figure 14, but for a $v_\phi = 0$ run. No rotation signature from the outflows and the protostellar disk is observed.

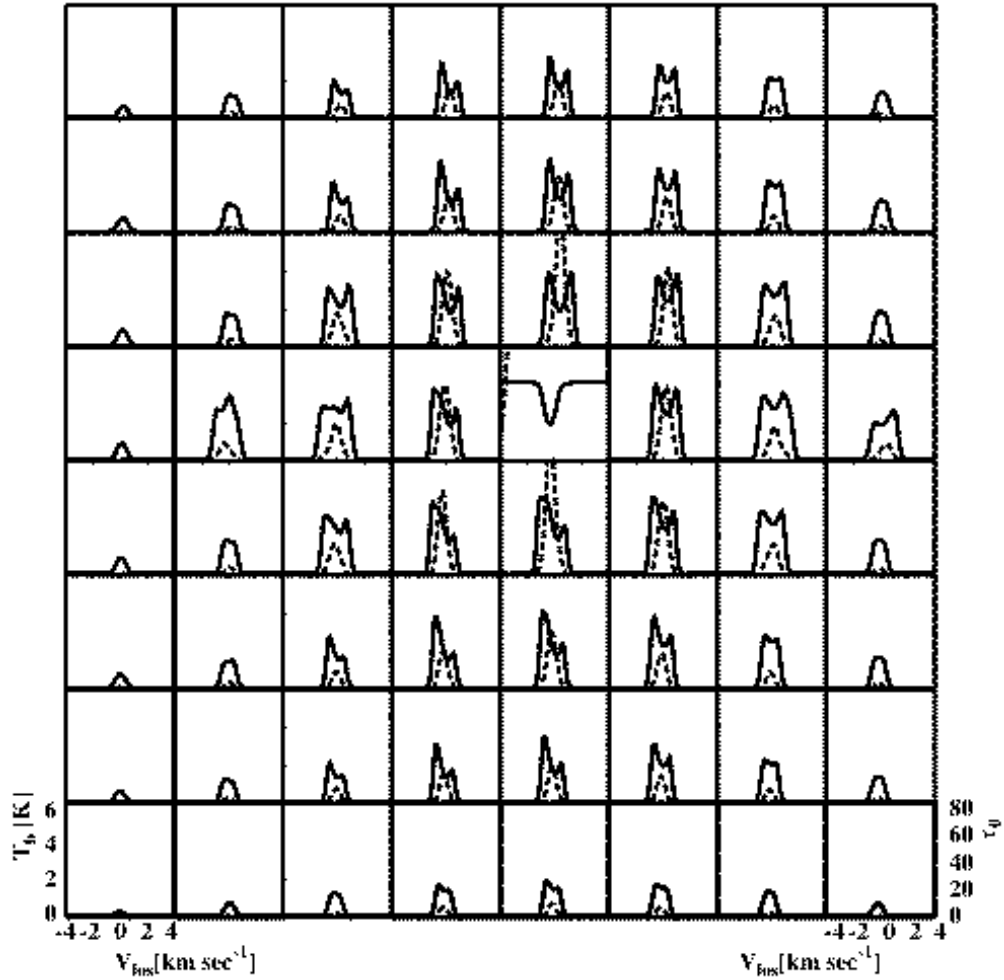


Fig. 16.— Line profile distribution of SiO(7 – 6) for a $\theta = 30^\circ$ view are sampled by ~ 300 AU spacing over the entire field-of-view. Solid lines denote intensity profiles, and dashed lines are optical thickness on the same line of sight. Line profiles in double-horn shape are almost ubiquitously seen in this view with varying relative ratio of red and blue peaks.

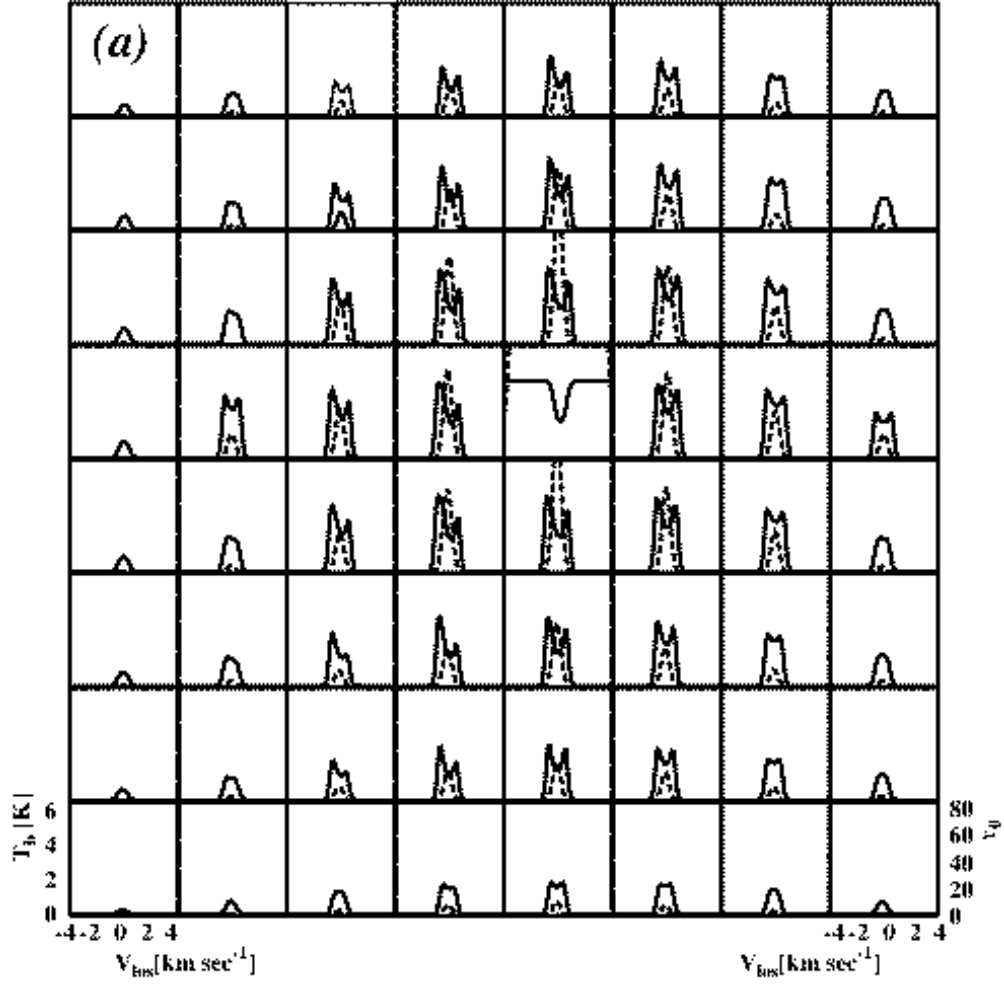


Fig. 17.— The same distribution maps of line and optical thickness profiles as Figure 16, but for the experimental results for case A (panel (a): radial velocity only) and B (panel (b): z -component of \mathbf{v}_{out} only). See text for details. Panel (a) shows the blue-skewed double-horn profiles almost in the entire field-of-view, and panel (b) represents symmetric double-horn profiles in the outflow region.

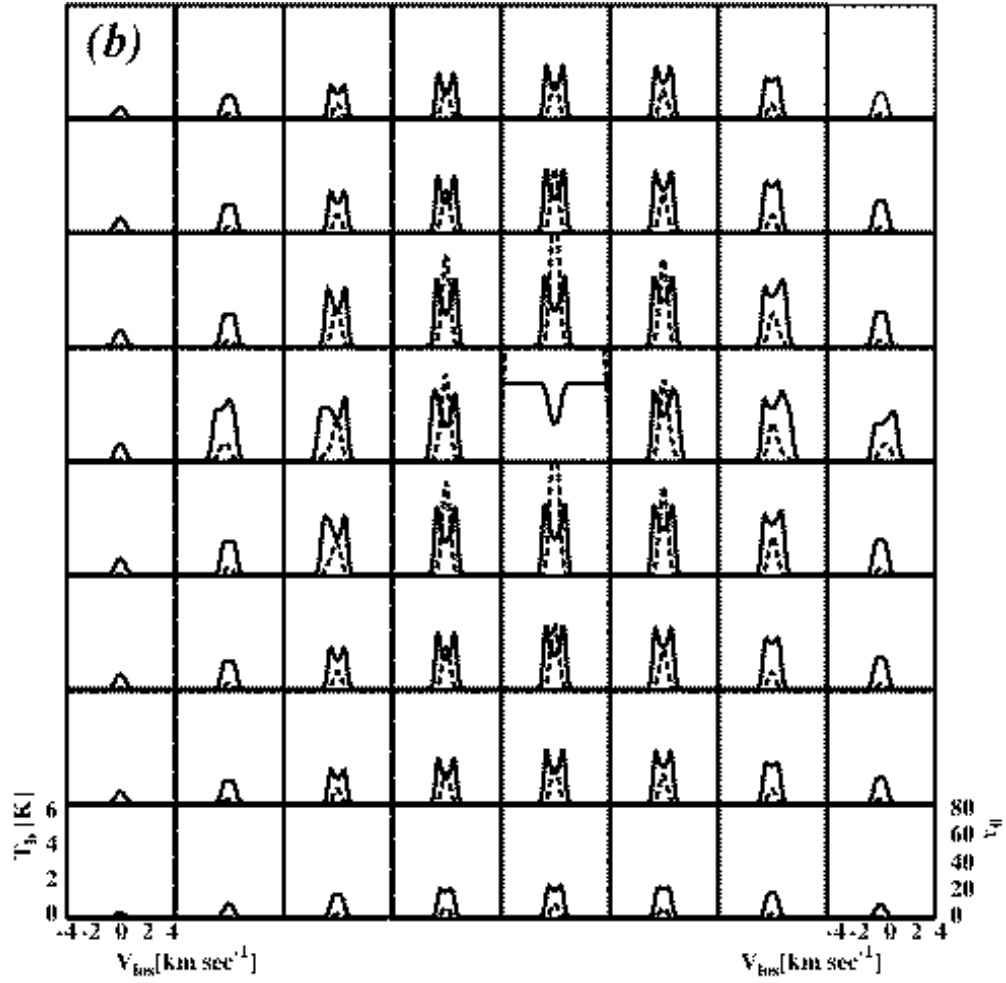


Fig. 17 cont.— Line and optical thickness profile distribution for the case B experiment (see text).

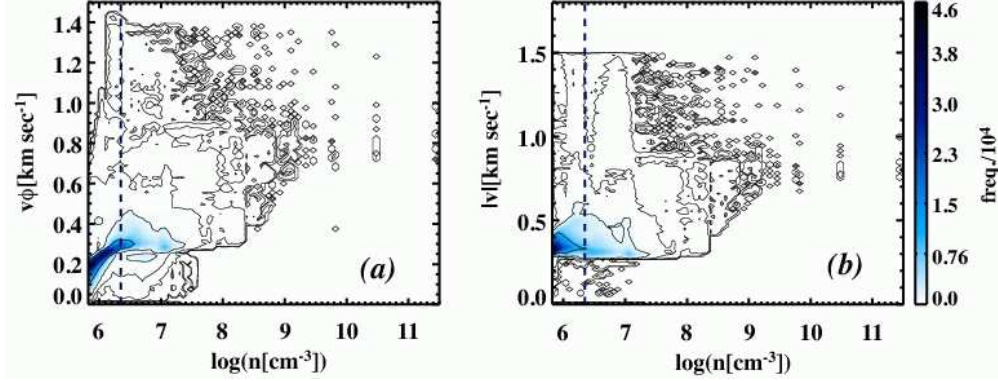


Fig. 18.— Velocity structure of the adopted snapshot data in two-dimensional PDF. Panel (a) shows the relation between v_ϕ and density, and panel (b) shows that of $|v|$ and density in both color scale and contours ($0, 10^0, 10^1, 10^2, 10^3,$ and 10^4).

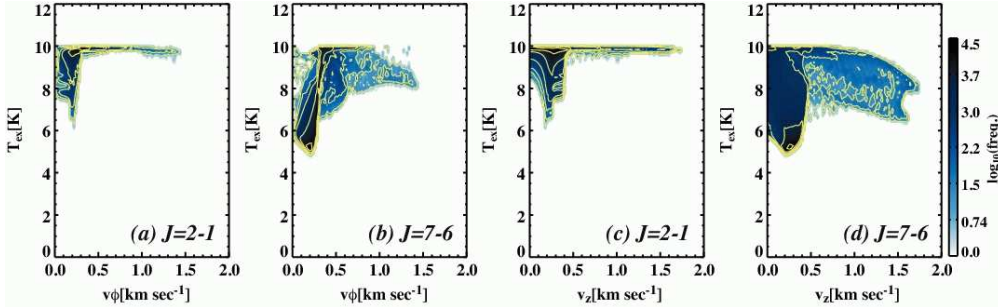


Fig. 19.— Relations between bulk velocity structure of the snapshot and excitation temperatures of SiO($2 - 1$) and ($7 - 6$) lines are shown in two-dimensional PDFs (solid contours are $0.0, 0.75, 1.5, 2.25, 3.0, 3.75$). Panels (a) and (b) describe the relation of T_{ex} and v_ϕ , and panels (c) and (d) describe that of T_{ex} and v_z . Higher J line shows a broader scatter for either of v_ϕ and v_z , and has a higher possibility of self-absorption compared to lower J line.

